AD-A072 589 MICHIGAN UNIV ANN ARBOR DEPT OF ATMOSPHERIC AND OCE--ETC F/G 8/10
NUMERICAL SIMULATION STUDIES FOR THE OCEANIC ANOMALIES IN THE N--ETC(U)
FEB 77 J C HUANG N00014-76-C-0141
NL

UNCLASSIFIED

1 OF 2

AD
A072589

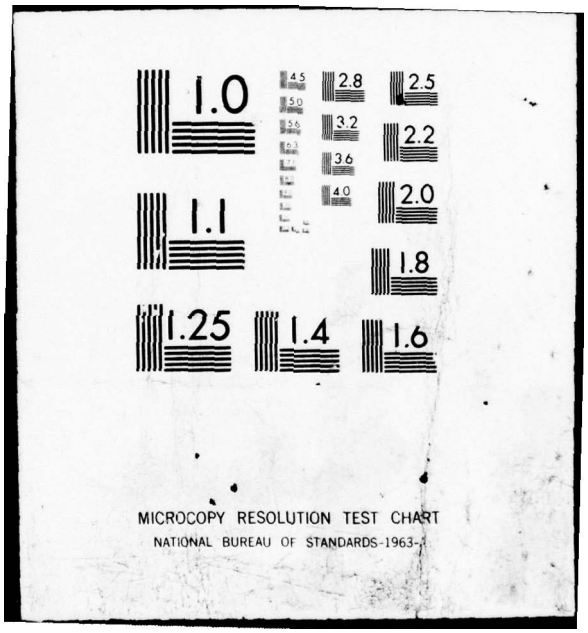
1.0
1.1
1.25
1.4
1.6
1.8
2.0
2.2
2.5
2.8
3.2
3.6
4.0
4.5
5.0
5.6
MICROCOPY RESOLUTION TEST CHART
NATIONAL BUREAU OF STANDARDS-1963-

Numerical Simulation Studi the Oceanic Anomalies in th North Pacific Basin

I. The Ocean Model and the Long-Term M

JOSEPH CHI HAN HUANG

February 1977

Office of Naval Research
U.S. Department of the Navy
Contract No. N00014-76-C-0141
Arlington, Virginia

Department of Atmospheric and Oceanic S

THE UNIVERSITY OF MICHIGAN

COLLEGE OF ENGINEERING
Department of Atmospheric and Oceanic Science

(12) 100 p.

(9) Final Report.

(6) NUMERICAL SIMULATION STUDIES FOR THE OCEANIC ANOMALIES IN THE NORTH PACIFIC BASIN.

I. The Ocean Model and the Long-Term Mean State.

AD A067839

by

(19) Joseph Chi Han/Huang

DRDA Project 014313

under contract with:

OFFICE OF NAVAL RESEARCH
U.S. DEPARTMENT OF THE NAVY
CONTRACT NO. N00014-76-C-0141
ARLINGTON, VIRGINIA
(15)

administered through:

DIVISION OF RESEARCH DEVELOPMENT AND ADMINISTRATION ANN ARBOR

(11) Feb[illegible]1977

Abstract

A time dependent, three-dimensional numerical dynamic model of the North Pacific Ocean, possessing an actual coastal configuration and ten layers, has been developed in order to show the physical nature of the large-scale normal and abnormal characteristics of the ocean in response to the various normal and anomalous seasonal meteorological conditions. Based on the simulated energetics, emphasis is given to identify the major physical processes and essential dynamic mechanisms responsible for the generation, evolution, and dissipation of large-scale anomalies in the North Pacific Ocean. The model is based on time integrations of the finite difference forms of the primitive equations. The oceanic circulation is driven by atmospheric forcing, namely, the surface wind stresses and the differential heating over the ocean. The flux form of numerical scheme for energy conservation and the rigid-lid approximation for filtering out the external inertia-gravity wave are used in the formulation.

The model has run for more than 80 years, simulated with the annual mean atmospheric data as the forcing boundary conditions. The long-term mean state in the model reveals the large-scale features of the circulation patterns and density distributions in the North Pacific Ocean. Three gyres, one large anticyclonic in the subtropical region and two smaller ones in the subartic and in the tropic region, are well developed. The total transport near the western boundary reached 56 Sverdrups, which agrees quantitatively well with observed mean transport in the Kuroshio Current south of Japan. All the equatorial currents, the Oyashio Current.

the Alaska Current, the west wind drift, and the California Current are grossly shown. Upwelling is observed along both the equator and the western boundary. Temperature and salinity distributions, except in high latitudes, compare well with observational atlas and field data.

Further experiments for the time-dependent, season fluctuations and for the thermal anomaly dynamics in the North Pacific Ocean have been carried out and will be reported in succeeding papers.

1. Introduction

In recent years, the substantial deviations of sea-surface temperatures from their long-term means, i.e., the thermal anomalies in the ocean, have attracted the attention of many oceanographers and meterologists. These anomalous phenomena, together with their temporal correlations and their spatial teleconnections with oceanic and atmospheric changes, have been extensively studied by Bjerknes (1962, 1966, 1969, 1972), by Namias (1959, 1965, 1969, 1970), and by others (e.g., Petterssen, et al., 1962; Rodewald, 1963). The general conclusions ascertain that the thermal anomalies in the ocean are constantly modifying the overlying atmospheric circulation, thereby altering the wind systems and the weather patterns. Observations indicate that climatic fluctuations in the ocean and atmosphere occur in all parts of the world at all times (Namias, 1965). In the Pacific Ocean, field data from the North Pacific Experiment (NORPAX) have shown that large temperature anomalies with intensities sometimes as high as 2°C to 5°C frequently occupy one-third to one-half or more of the North Pacific Ocean, and they usually persist for long periods of time. Besides their possible feedback to the atmosphere, the anomalies cause abnormal advections which, together with the atmospheric anaomalous variations, influence the general oceanic circulation patterns (Namias, 1965, Arthur, 1966). For example, in 1957-1958 an anomalous sea surface temperature in the Pacific was associated with the weakening of the California Current, and forced it to swing offshore (Isaacs, 1968). This resulted in a strong invation of warm, subtropical water into the west coast as far

north as British Columbia.

The physical natures of the atmosphere, the ocean, and the biota therein are closely coupled and mutually interacting. In the large-scale air/sea interactions the ocean primarily supplies heat to the atmosphere while the atmosphere supplies momentum and heat to the ocean. The heat released from the ocean modifies the atmospheric circulation while the momentum and heat exchange from the atmosphere to the ocean determine the flow pattern and heat content in the ocean. The oceanic circulation, then, redistributes the thermal energy, thereby setting up a closed feedback system between the ocean and the atmosphere. For the purpose of studying the mutual effects and their teleconnections in the ocean/atmosphere system, it is indispensible to employ an ocean/atmosphere coupled system. In a pioneering work, Manabe (1969) and Bryan (1969a) performed the first numerical experiment of an ocean/atmosphere model that included major coupling and mutual adjusting mechanisms. Their results showed that the poleward transport of heat by oceans reduced the atmosphereic meridional heat transport, which in turn decreased the baroclinic instability in the troposphere. In the tropics, the oceanic effect changed the rainfall distribution and influenced the strength of the Hadley circulation producing more realistic results. Therefore, the coupled model did demonstrate its ability to more accurately portray the large-scale features in the atmosphere.

Simulation studies of the ocean have been successfully carried out by Takano (1969), Il'in, et al. (1969), O'Brien (1971), Bye and Sag (1972), Bryan and Cox (1972), and Holland and Hirschman (1973). These

have taken into account realistic configurations of the basins under their investigation with a simplified formulation of the systems. Bryan (1963, 1969b), Gormatyuk and Sarkisyan (1965), Bryan and Cox (1967, 1968), Crowley (1970), and Haney (1974) have taken the complete dynamics into their models of certain idealized domains. Cox (1970) has used Bryan's model (1969b), which includes the whole dynamics as well as the irregular boundaries, to investigate the monsoon effect in the circulation patterns in the Indian Ocean.

Though it is not realistic to employ a regional atmospheric model for studies of planetary responses and global teleconnections, a regional ocean model is tolerable for dynamic studies in the ocean due to its solid boundary enclosement and the semi-isolated characteristics of certain basins. If one addresses the more specific problems of physical processes, thermal structures and dynamic responses in an ocean under meteorological forcing, it is probably feasible to examine a semi-enclosed domain such as the North Pacific Ocean.

In the investigation of the anomalous state in the ocean, the anomalies can be considered as the perturbation quantities, though not necessarily very small, superimposed upon the basic long-term averages. In general, the oceanic anomalies are, at least to the lower order of approximation, generated by the atmospheric anomalies, such as the anomalous pressure, the anomalous wind, the anomalous heat-exchange and water flux. An approximate method for estimating the large-scale sea-surface temperature anomalies due to atmospheric changes, proposed by Namias (1965) and extended by Arthur (1966) and Jacobs (1967), has shown some

degree of success.

We have investigated the anomaly dynamics in the North Pacific Ocean by numerical simulation. The ocean model we developed for the anomaly study considers the actual configuration of the North Pacific Ocean and takes the complete dynamic equations with all large-scale physical processes into consideration. The basic numerical scheme used in the model is a modification of Haney's idealized ocean model (1974). The space-staggered grid and the spacing differencing scheme used in the present model follows that of the UCLA atmospheric general circulation model (Gates, et al., 1971). In addition, the present model treats the upper boundary conditions in an improved manner. The variation of heat flux between the ocean and the atmosphere is not only a function of the coupled air-sea temperatures but also a summation of all heating and interacting components calculated from empirical formulae for the heat balance at the naviface. In computing wind stress, the near surface atmospheric stability is also taken into consideration. Both the longitudinal component and the meridional component of wind stress are used as the boundary conditions in the momentum equation. Furthermore, since it is well-known that salinity plays an important role in the ocean dynamics at high latitudes, a prognostic equation for salinity conservation is also included in the hydrodynamic system.

Our study is originated from the objective of NORPAX to understand the low-frequency fluctuations in the upper layer of the North Pacific Ocean and their relations to the overlying atmosphere. The major goal is to investigate the anomaly dynamics and to describe the configuration

and evolution of the thermal anomalies in the North Pacific by numerical simulations. Because the anomalies are generally small, it is necessary to take a systematic step-by-step approach, from the spin-up of an ocean model to the final anomaly experiments. A set of three papers are in progress to report the sequence of numerical dynamic study for the North Pacific Ocean. This first paper describes briefly the basic physics in the numerical model which is the basic tool for our thermal anomaly investigations, and shows the simulated long-term mean state in the North Pacific Ocean. Our major interest is in the large-scale (more than 1000 km) and long-term (months to years) fluctuations in the North Pacific Ocean in relation to the overlying atmosphere. The following paper, II, will present the seasonal fluctuations in the North Pacific Ocean, and III will discuss the dynamic mechanisms and results of anomaly experiments based on real-time specifications in the North Pacific model.

2. The dynamic model

The formulation of the model is based on the primitive equations relative to the right-hand spherical coordinate system (λ,ϕ,z) on the surface of the earth with z taken positive upward from the mean sea level. The Navier-Stokes equations for incompressible and nonhomogeneous fluid with some basic physical approximations, namely, the Boussinesq approximation, the hydrostatic approximation, the eddy viscosity approximation, and the traditional approximation (Eckart, 1960), are integrated with time. Let (u,v) be the horizontal component of velocity V and define an advective flux operator as:

$$\mathcal{L}(q) = \frac{\sec\phi}{a}\left[(uq)_\lambda + (vq\cos\phi)_\phi\right] + (wq)_z \tag{1}$$

where q is any scalar quantity. With all symbols as defined in Table 1, the governing equations are:

$$u_t = \mathcal{L}u + v\sin\phi(2\Omega+a^{-1}u\sec\phi) - (\rho_o a)^{-1}\sec\phi p_\lambda + F^\lambda \tag{2}$$

$$v_t = \mathcal{L}v - u\sin\phi(2\Omega+a^{-1}u\sec\phi) - (\rho_o a)^{-1}p_\phi + F^\phi \tag{3}$$

$$p_z = -\rho g \tag{4}$$

$$a^{-1}\sec\phi[u_\lambda+(v\cos\phi)_\phi] + w_z = 0 \tag{5}$$

$$T_t = \mathcal{L}T + Q \tag{6}$$

$$S_t = \mathcal{L}S + H \tag{7}$$

$$\rho = \rho(T,S,p) \tag{8}$$

where all alphabetic subscripts denote partial derivatives and

$$F^{\lambda} = \nu_1[\nabla^2 u + a^{-2}(1-\tan^2\phi)u - 2a^{-2}\tan\phi\sin\phi v_{\lambda}] + \nu_2 u_{zz} \tag{9}$$

$$F^{\phi} = \nu_1[\nabla^2 v + a^{-2}(1-\tan^2\phi)v + 2a^{-2}\tan\phi\sin\phi u_{\lambda}] + \nu_2 v_{zz} \tag{10}$$

$$Q = k_1\nabla^2 T + h^{-1}k_2 T_{zz} \tag{11}$$

$$H = k_1\nabla^2 S + h^{-1}k_2 S_{zz} \tag{12}$$

wherein

$$\nabla^2(q) = a^{-2}\sec^2\phi q_{\lambda\lambda} + a^{-1}\sec\phi(a^{-k}\cos\phi q_{\phi})_{\phi} \tag{13}$$

Following Bryan (1969b), the step function $h(-\rho'_z)$ in (11) and (12) incorporates the convective density adjust mechanism wherein ρ' indicates the potential density of the ocean water. Notice that, although in most cases the vertical column of the oceanic water is stable, static instability due to inversions in the potential density stratification can occur at any level and cause strong vertical mixing in the ocean. Nevertheless, most of the unstable phenomena happen in the surface layers where all the atmosphere-ocean interactions and energy transformations occur. Since the static instability in the real ocean lasts only for a short period of time (hours), the simplest way of treating it is an instantaneous convective density adjustment mechanism. Whenever the instability is detected between layers, a quasi-homogeneous mixed density of marginal stable lapse rate is assumed for all unstable adjacent layers.

The boundary conditions for the lateral and bottom solid boundaries

are zero normal velocity, and zero normal heat or salt flux on solid boundaries,

$$W_n, T_n, S_n = 0 \tag{14}$$

where n denotes differentiation along the normal of the boundary surface. On the equatorial southern boundary in addition to the no normal velocity and no normal fluxes of heat and salt, the tangential free-slip condition is also imposed,

$$v, u_\phi, T_\phi, S_\phi = 0 \quad \text{at} \quad \phi = 0 . \tag{15}$$

Note that the bottom topography and the geothermal heat flux have been neglected at the lower boundary in this preliminary study. It is known that the bottom topography is important to the vertically integrated transport and can influence the path of the western boundary current in the ocean (Warren, 1963; Holland, 1967; Schulman and Niiler, 1970; O'Brien, 1971). But we are more interested in the anomalous phenomena existing generally in the upper shallow layer of the ocean where the baroclinic velocity field may not be markedly affected by topography.

At the upper surface of the ocean, the "rigid-lid" approximation (Bryan, 1969b) is employed in order to gain a more efficient time-dependent calculation.

Other upper surface boundary conditions are:

$$\nu_2(u_z, v_z) = \frac{1}{\rho_o}(\tau^\lambda, \tau^\phi) \tag{16}$$

where τ^λ, τ^ϕ are the longitudinal and the latitudinal components of the

surface stress:

$$\kappa_2 S_z = S_1(E-R) \tag{17}$$

where E - R is the net difference of evaporation and precipitation; and

$$\kappa_2 T_z = \frac{Q_S}{\rho_o C} \tag{18}$$

where Q_s is the net downward heat flux across the atmosphere/ocaen interface and C is the specific heat of water at constant pressure. A detailed description of atmospheric forcing function, namely, the wind stresses and heating is in the next section.

The boundary conditions of zero normal flow and zero heat and salinity fluxes through the lateral boundaries, zero vertical velocity at the balanced upper surface and at the bottom guarantee the satisfaction of integral constraints for mass, momentum, and energy.

The wind stress and the heat flux. The synoptic net downward heat flux, according to the heat balance equation at the naviface, can be written as

$$Q_S = Q_I - Q_B - Q_H - Q_E \tag{19}$$

Where Q_I is the net downward flux of solar insolation and Q_B, Q_H, Q_E are upward fluxes of infrared radiation, sensible heat and latent heat, respectively, as defined in Table 1. Table 1 also defines all other notations used in the following formulae.

The solar radiation flux can be calculated from a simplified formula with empirical constants obtained from the atmospheric climatology

(Johnson, et al., 1958; London, 1957; Vonder-Haar and Hanson, 1969) as

$$Q_I = 0.95\, Q_o(0.74-0.6N_c) \ . \tag{20}$$

The net upward infrared heat flux is calculated from

$$Q_B = 0.985\, cT_S^{\,4}(0.39-0.06\, e_a^{\,1/2})\ (1-0.6\, N_c^{\,2}) \ . \tag{21}$$

The sensible and latent heat are computed from

$$Q_H = \rho_a\, C_H\, C_a\, |W_a|\ (T_s-T_a) \tag{22}$$

and

$$Q_L = \rho_a\, C_E\, L\, |W_a|\ (q_s-q_a) \tag{23}$$

where $|W_a|$ is the wind speed at 10 m above the surface. The specific humidity is related to the vapor pressure by

$$q = \frac{.622}{P_a}\, e \tag{24}$$

where P_a is the mean atmospheric surface pressure. The saturated vapor pressure at the ocean surface temperature can be calculated from the Clausius-Clapeyron equation (Hess, 1959).

$$\mathrm{Log}_{10}\, e_s = (9.4051-2353/T_s) \ . \tag{25}$$

The momentum flux at the ocaen-atmosphere interface is expressed as the surface wind stresses,

$$(\tau^{\lambda},\tau^{\varphi}) = \rho_a\, C_p\, |W_a|\ (u_a,v_a) \tag{26}$$

where (u_a, v_a) are components of $\mathbf{V}_a$. Following Deardorff (1968) and using data of Bussinger, et al. (1971), the exchange coefficients of heat, water, and momentum are function of atmospheric stability as,

$$\left.\begin{aligned} C_D &= (C_D)_N \exp(-2\,\beta_v\,Ri) \\ C_H &= C_E = (C_H)_N \exp[-(\beta_v+\beta_T)Ri] \end{aligned}\right\} \text{for stable cases } (Ri > 0) \tag{27a}$$

$$\left.\begin{aligned} C_D &= (C_D)_N \left[1 + \frac{7}{b_1} \ln (1-b_1\,Ri)\right] \\ C_H &= C_E = (C_H)_N \left[1 + \frac{11}{b_2} \ln (1-b_2\,Ri)\right] \end{aligned}\right\} \text{for unstable cases } (Ri < 0) \tag{27b}$$

where Ri is the bulk Richardson number, a parameter to measure the stability of the atmosphere,

$$Ri = \frac{gZ_{10}}{T_{vo}V_a^2}\left[(T_a-T_s) + 0.38\,T_a\,\frac{e_a-e_s}{P_a}\right], \tag{28}$$

wherein β_v, β_T, $(C_D)_N$, b_1, b_2, Z_{10}, and T_{vo} are constants (Bussinger, et al., 1971) as listed in Table 2. The coefficient of water particle exchange is assumed to be the same as that of the exchange of heat. All values of atmospheric parameters are provided by Fleet Numerical Weather Central at Monterey, California.

The hydrostatic equation. The equations of state defines the density in terms of temperature, salinity, and pressure. The departure of pressure at any level in the ocean from the vertically averaged pressure is uniquely determined by the density. Integrating the hydrostatic equation downward with respect to the vertical coordinate, we obtain

$$p'(z) = \int_z^0 \rho g dz - \frac{1}{D} \int_{-D}^0 \left(\int_z^0 \rho g d\xi \right) dz \ . \tag{29}$$

The vorticity equation. The exclusion of kinematic surface variations makes the surface pressure impossible to calculate. Instead we compute the shear velocity components (u',v') as prognostic variables with the pressure terms substituted by the hydrostatic equation. The vertical mean velocity $(\hat{u},\hat{v})$ is obtained from the stream function by solving the vorticity equation. The total velocity is, then, the combination of the vertical mean velocity and the deviation from the vertical mean, i.e.,

$$(u,v) = (\hat{u}+u',\hat{v}+v') \ . \tag{30}$$

The surface and bottom boundary conditions on w permit us to define the nondivergent vertically integrated stream function which satisfies the continuity equation,

$$\hat{u} = a^{-1} \psi_\phi \tag{31}$$

$$\hat{v} = a^{-1} \sec\phi \psi_\lambda \tag{32}$$

where, for any scalar q,

$$(\hat{q}) = \frac{1}{D} \int_{-D}^0 (q) dz \tag{33}$$

is the vertically integrated mean. Then the predictive vorticity equation can be obtained by eliminating pressure terms in (2), (3) as

$$\nabla^2 \psi_t = \frac{\sec\phi}{a} \{ (\hat{G}^\phi + \hat{F}^\phi)_\lambda - [(\hat{G}^\lambda + \hat{F}^\lambda)\cos\phi]_\phi \} - \frac{\sec\phi}{a^2} f_\phi \psi_\lambda \tag{34}$$

where f is the Coriolis parameter and

$$G^{\lambda} = u + \frac{uv}{a}\tan\phi \tag{35}$$

$$G^{\phi} = v - \frac{uv}{a}\tan\phi \tag{36}$$

The shear current. The predictive equations for the vertical shear current (u',v'), from (2) and (3), subtracting their respective vertical means, become

$$u'_t = \frac{-\sec\phi}{\rho_o a} p'_{\lambda} + fv' + F^{\lambda} + G^{\lambda} - (\hat{F}^{\lambda}+\hat{G}^{\lambda}) \tag{37}$$

$$v'_t = \frac{-1}{\rho_o a} p'_{\phi} - fu' + F^{\phi} + G^{\phi} - (\hat{F}^{\phi}+\hat{G}^{\phi}) \tag{38}$$

where p' is defined in (29).

It is obvious from (37) and (38) with the definition of the vertical mean (33) that

$$(\hat{u}'_t,\hat{v}'_t) = 0 . \tag{39}$$

With the initial condition $(u',v') = 0$ at $t = 0$, then, it is always true that

$$(\hat{u}',\hat{v}') = 0 . \tag{40}$$

The prognostic variables are u', v', ψ, T, and S predicted from (37), (38), (34), (6), and (7), respectively. The diagnostic variables are w, ρ, p obtaining from (5), (8), and (29), respectively.

3. Finite difference equations

The basic approach for arriving at the solutions is that the system of partial differential equations and boundary conditions in the continuum are approximated by a set of finite-difference equations and bounary conditions. As the grid size approaches zero, the finite difference solution obtained with any convergent scheme will approach the true solution. However, since no infinitesimal grid size is used in practice, the finite difference scheme chosen to compute the solution must be capable of economically reaching the statistical asymptote of the true solution. In numerical simulations the governing equations are integrated beyond the limit of mathematical justification based on local accuracy. Therefore, it is vitally important that certain integral constraints such as the conservation of total kinetic energy during adiabatic and nondissipative processes and the conservation of total entropy and total potential enthalpy during adiabatic processes are maintained. In the construction of the model, we have used the quadradic conserving method (Arakawa, 1966; Bryan, 1969b) to maintain the conservation of integral constraints.

In the NORPAX model, the actual configuration of the North Pacific Ocean is taken into account by approximating the coastline with the meridians or the latitude-circles passing through the nearest grid points as shown in Figure 1. The origin of the coordinates is taken at the intersection of the mean sea surface, the equator, and the western boundary of the ocean (λ_o = 120°E). The whole North Pacific domain is from 120°E to 80°W in longitude and from 0°N to 65°N in latitude with a constant depth

of 4 km. The vertical coordinate z is set for 10 variable-thickness layers as shown in Figure 2. If z denotes the height, negative below the surface, the thicknesses between the levels are defined as

$$\Delta z_{1/2} = -2z_1 ,$$

$$\Delta z_{k+1/2} = Z_{k-1} - z_k, \quad k = 2,\ldots,K , \tag{41}$$

$$\Delta z_{k+1/2} = 2(z_K + D)$$

where D is the total depth. The thickness of the kth level is defined as

$$\Delta z_k = \frac{1}{2}(\Delta z_{k-1/2} + \Delta z_{k+1/2}), \quad k = 1,\ldots,K . \tag{42}$$

The analog to (33) is

$$\hat{q} = \frac{1}{D}\sum_{k=1}^{K}(q)\,\Delta z_k . \tag{43}$$

A computational box is one subvolume of the ocean with a finite angular difference of $\Delta\lambda$ in the longitudinal direction and $\Delta\phi$ in the meridional direction is shown in Figure 3. We have defined

$$\Delta x_{j'} = a\cos\phi_{j'}\Delta\lambda ,$$

$$\Delta y = a\Delta\phi \tag{44}$$

where j' may refer to the integer grid points or to the half integer grid points. Notice that, based on the definition of (44), the x-component is equivalent to λ-component and y-component is equivalent to ϕ-component.

Since the computation is carried out in flux form, the areas constituting one subvolume in the ocean can be designated as

$$A_1 = \Delta y \Delta z_k ,$$

$$A_2 = \Delta x_{j'} \Delta z_k , \tag{45}$$

$$A_3 = \Delta x_{j'} \Delta y .$$

The subvolume under computation is

$$\sigma_{j',k} = \Delta x_{j'} \Delta y \Delta z_k . \tag{46}$$

For convenience, let us define

$$\bar{q}^{\ell} = \frac{1}{2} [(q)_{\ell+1/2} + (q)_{\ell-1/2}] \tag{47}$$

and

$$\delta^{\ell}(q) = [(q)_{\lambda+1/2} - (q)_{\ell-1/2}] \tag{48}$$

where ℓ may be any of the spatial indices. For instance,

$$\delta^{i}(\bar{\Psi}^{j})_{i+1/2,j+1/2} = \frac{1}{2} (\Psi_{i+1,j+1} + \Psi_{i+1,j}) - \frac{1}{2} (\Psi_{k,j+1} + \Psi_{i,j}) .$$

There are five prognostic variables, u', v', ψ, T, S and three diagnostic variables, w, ρ, and p in the model. In consistence with the requirements for integral constraints, the space-staggered grids are arranged in such manner that T, S, and ρ are basically computed at the integer grid points (i,j,k); u,v at the half integer points (i+1/2, j+1/2,k); w at the (i,j,k+1/2) point. The stream function ψ is

two-dimensional and is computed at the (i,j) points. All variables are subscripted according to their spatial positions and are superscripted with the time step n, e.g., $T^n_{i,j,k}$. The horizontal placement of variables is also shown in Figure 3. All variables needed at points other than the basic grid points during the computation process are usually defined by the average values of the parameter at the immediately available points surrounding the temporarily required point. For example

$$u_{i+1/2,j,k} = \bar{u}^{j}_{i+1/2,j,k} .$$

Momentum equations. The finite difference equations analogous to (37) for the x-component of the vertical shear current with respect to the (i+1/2,j+1/2,k) subvolume can be written as,

$$(u'\sigma)^{n+1} - 2b\Delta t f(v'\sigma)^{n+1} = A \tag{49}$$

where b is the implicit stabilizing factor for the Coriolis terms, t the unit time step and

$$A = (u'\sigma)^{n-1} + 2\Delta t(1-b)\, f(v'\sigma)^{n-1} + 2\Delta t\, (B^n + F^{n-1} + G^n - \hat{U}) \tag{50}$$

The pressure gradient force is approximated from density alone according to (29) as,

$$B = -\delta^i(\bar{p}^j)\,\frac{A_1}{\rho_o} \tag{51}$$

where

$$P = \begin{cases} 0, & k = 1 \\ \sum_{k=1}^{K-1} \rho^{-k}_{k+1/2}\, g\Delta z_{k+1/2}, & k = 2,\ldots,K \end{cases} \tag{52}$$

The friction terms, according to (11) are,

$$F = \frac{\nu_1 A_1}{\Delta x}\delta^i(\delta^i u) + \frac{1}{\Delta y}\delta^j(\nu_1 A_2 \delta^j u) + \frac{\delta^k}{\Delta z}(\nu_2 A_3 \delta^k u) + \nu_i\left[(1-\tan\phi)\frac{u\sigma}{a^2} - \frac{2\tan\phi\, A_1 \delta^i(\bar{v}^i)}{a^2\cos\phi}\right]. \tag{53}$$

The nonlinear terms, according to (1) and (35) are,

$$G = -\delta^i\{\bar{u}^i[(\overline{\bar{u}^i A_1}^{\,i})^{\,j}]\} - \delta^j\{\bar{u}^j[(\overline{\bar{v}^i A_2}^{\,j})^{\,i}]\} + \delta^k\{\bar{u}^k[\overline{\bar{w}^j A_3}^{\,i}]\} - uv\delta^j A_2 \tag{54}$$

Note that the right-hand side of (54) is, except the last term, the negative form of the flux operator $\mathcal{L}$. The vertically averaged term is

$$\hat{U} = \frac{1}{D}\sum_{k=1}^{K}(B^n + F^{n-1} + G^n)\Delta z_k . \tag{55}$$

A prognostic equation for the v'-equation according to (38) is,

$$(v'\sigma)^{n+1} + 2b\Delta t f(u'\sigma)^{n+1} = A^* , \tag{56}$$

Where A* is similar to A, B*, F*, G* is similar to B, F, G, and $\hat{V}$ is similar to $\hat{U}$.

Thus the shear current at all half grid points (i+1/2, j+1/2, k) are,

$$(u')^{n+1} = G + 2b\Delta t f G^* / (1+4b(\Delta t)^2 f^2)\sigma \tag{57}$$

$$(v')^{n+1} = G^* - 2b\Delta t f G / (1+4b^2(\Delta t)^2 f^2)\sigma \tag{58}$$

Notice that in (57) and (58) the basic time differencing scheme used in the model is the leapfrog scheme. This time scheme can cause the temporal "splitting" phenomena in the solution for a long-term integration process (Lilly, 1965). Therefore, the implicit backward time scheme (Matsuno, 1966) is periodically used every 25 time steps. The Coriolis term is treated implicitly which permits a time step longer than the inertial period (Bryan, 1969b). For linear computational stability, a stabilizing factor b is chosen to provide a slight damping of inertial oscillations. b = 0.55 is used for the present run.

The finite diffence vorticity equation with respect to (i,j) points according to (34) is

$$\nabla^2(\psi D)_t = \delta^i\left[\overline{\frac{1}{\Delta x}(\hat{G}^*+\hat{F}^*)}\right]^j - \delta^j\left[\overline{\frac{1}{\Delta y}(\hat{G}+\hat{F})}\right]^i - \frac{1}{2}\delta^i f\delta^{2i}\psi \qquad (59)$$

where G, F, G*, F* are the vertically averaged mean of G^λ, F^λ, G^ϕ, F^ϕ equivalently shown in (53) and (54), $\delta^{2i}\psi$ indicates the derivative of center difference with a separation of $2\Delta x$, and

$$\nabla^2\psi = \delta^i\left[\overline{\frac{\Delta y}{\Delta x}\delta^i(\bar{\psi})^j}\right]^j + \delta^j\left[\overline{\frac{\Delta x}{\Delta y}\delta^j(\bar{\psi})^i}\right]^i \qquad (60)$$

This is a nine-point finite difference Lapacian operator which can easily be reduced to a five-point Lapacian operator if $\Delta x = \Delta y$. With $\psi_{i,j} = 0$ on all lateral boundaries, (59) is solved by over-relaxation in the interior with an initial guess of $\psi_t = 0$. The ψ^{n+1} is advanced from ψ^{n-1} in pace with the same time step of the vertical shear current.

The vertical mean velocity, with respect to the computed points (i+1/2,j+1/2) is,

$$\hat{u} = -\delta^{j}(\bar{\psi})^{i}/\Delta y \tag{61}$$

$$\hat{v} = \delta^{i}(\bar{\psi})^{j}/\Delta x \tag{62}$$

From the continuity equation the vertical velocity w can be obtained with respect to the (i,j,k) subvolume index as (i,j,k+1/2),

$$w_{k+1/2} = w_{k-1/2} - \frac{\Delta z}{\sigma}\left[A_1\delta^{i}(\bar{u}^{j}) + \delta^{j}(A_2\bar{v}^{i})\right] \tag{63}$$

where $w_{i,j,1/2} = 0$ at the surface. Note that the vertical velocity is diagnostically defined at the top and the bottom surface of the subvolume under consideration.

It is readily shown (Huang, 1973) that there is no false source or sink of kinetic energy using the above finite difference scheme.

Temperature and salinity equation. The temperature and salinity are calculated at all integer grid points (i,j,k). The finite difference form of the thermal energy equation is

$$(T\sigma)^{n+1} = (T\sigma)^{n-1} + 2\Delta t[Q^{n}+(Q^{*})^{n-1}] \tag{64}$$

where

$$Q = -[A_1\delta^{i}(\bar{T}^{i}\bar{u}^{j}) + \delta^{i}(A_2\bar{T}^{j}\bar{v}^{i})] + A_3\delta^{k}(\bar{T}^{k}w) \tag{65}$$

and

$$Q^{*} = \frac{\kappa_1 A_1}{\Delta x_j}\delta^{i}(\delta^{i}T) + \frac{1}{\Delta y}\delta^{j}[\kappa_1 A_2\delta^{j}T] - A_3\delta^{k}\left[\frac{\kappa_2}{\Delta z_{k+1/2}}\delta^{k}T\right]$$

where the eddy diffusivities may be treated as parameters depending on j and k.

Similarly, the finite difference equation for salinity analogous to (7) has exactly the same form if S is substituted for T. The only source and sink for the potential energy in the ocean domain, besides the small portion internally transformed from the kinetic energy, are the heat and water input through the naviface and the diffusive dissipations.

Boundary conditions. All the mesh grid points on the solid lateral boundaries, which are approximated by the meridians and by the latitude circles passing through the nearest integer grid points, coincide with the calculating points ψ, T, and S. Understanding that the other two dummy indices are not specified, the zero flux condition at all solid boundaries lead to

$$q_{\ell+1} = q_{\ell-1} \tag{66}$$

where q is the variable (T,S) computed at the boundary and ℓ is the index normal to the boundary at the boundary such as i*, I, and J. However,

$$\psi_{i,j} = 0 \tag{67}$$

at all lateral boundaries. The no-slip boundary condition leads to

$$(u,v)_{\ell+1/2} = -(u,v)_{\ell-1/2} . \tag{68}$$

However, for the longitudinal flow at the southern boundary, the free slip boundary condition is also used. That is, for j indices,

$$(u,v)_{1/2} = (u,-v)_{3/2} \tag{69}$$

The downward fluxes of heat, water, and momentum through the naviface are parameterized as the upper boundary conditions indexed at k = 1/2,

$$\frac{\kappa_2}{\Delta z_{1/2}} \delta^k T_{1/2} = \frac{Q_s}{\rho_o C} , \tag{70}$$

$$\frac{\kappa_2}{\Delta z_{1/2}} \delta^k (S)_{1/2} = S_1 (E-R) , \tag{71}$$

$$\frac{\nu_2}{\Delta z_{1/2}} \delta^k (u,v)_{1/2} = \left(\frac{\tau^\lambda, \tau^\phi}{\rho_o}\right) . \tag{72}$$

Hydrostatic stability. At places where excessive upward heat flux occurs and where evaporation exceeds precipitation by a large amount, a layer of heavy cold and salty water will be formed in the upper layers of the ocean. Whenever the local lapse rate of density is less than the vertical lapse rate which will ensure a marginally stable vertical density distribution, the hydrostatic instability exists in the adjacent layers. Since instability in the real ocean usually lasts for a short period of time, an instantaneous convective adjustment mechanism is activated in the model. Let

$$\gamma_\rho = -\left(\frac{\rho_{k-1} - \rho_k}{\Delta z_{k-1/2}}\right) \tag{73}$$

be the equivalent lapse rate of density between layers. A small positive value, ϵ_ρ, is assumed since there may exist a slight inversion in density within the marginal stable limit. In the model the lapse rate between layers is computed and compared with ϵ_ρ. If

$$\begin{aligned} -\gamma_\rho > \epsilon_\rho \qquad & \text{stable} \\ -\gamma_\rho < \epsilon_\rho \qquad & \text{unstable} \end{aligned} \tag{74}$$

where ϵ_ρ is estimated from the average density distribution in the ocean. Assuming the contribution to the density variation from the temperature and from the salinity are equally important, the marginally stable criteria for temperature and salinity can be estimated from ϵ_ρ and the coefficients for temperature and salinity expansions in the mean state of ocean. Then, in case instability is detected between layers, the temperature, salinity, and density in these vertical layers are mixed into quasi-homogeneity. For instance, if instability exists in layer k-1 and k, the adjusted temperature will be

$$T_k^* = \frac{T_k \Delta z_k + (T_{k-1} - \epsilon_T \Delta z_{k-1/2}) \Delta z_{k-1}}{\Delta z_{k-1} + \Delta z_k}$$

$$T_{k-1}^* = T_k^* + \epsilon_T \Delta z_{k-1/2} \qquad (75)$$

where the superscript * indicates the adjusted value after mixing and ϵ_T is the marginal stable criterion for temperature. These stability criteria and the adjusting processes are applied to all layers in the column, and the procedure is repeated whenever there is more than one unstable subcolumn until stability has been reached for the whole column.

4. Results

Flexibility and efficiency. In simulation studies using finite difference schemes for long-term integrations, not only the conservation of integral properties and the accuracy of solution in the statistic sense are essential considerations, but the flexibility in choosing grid separations and the efficiency in carrying out the computation are also important factors in designing numerical experiments. For the flexibility of the model, we have programmed in such a manner that the whole domain is computed in a sequence of blocks which consist of many computational boxes independent of vertical layers. We may execute the experiment with one version of the model which possesses reasonably small space separations, as small as 20 km in both longitudinal and meridional directions with as many layers as needed. This is important in the long run for our purpose of carrying out much-finer-mesh experiments in the later state of our investigation which may involve the meso-scale dynamics. We also think our algorithm and computational sequences are optimized in such a manner that it took only 14 sec of CDC 7600 CPU for one model day with 2.5 degrees in horizontal and 10 layers in vertical. Depths of the ten levels of the 2.5-degree model are placed, respectively, at 10, 30, 60, 100, 150, 225, 350, 700, 1500, and 3000 m below the naviface and the constant maximum depth of the ocean is assumed at 4000 m as shown in Figure 2. It is obvious that much emphasis has been put on the column of water above the permanent thermocline.

Three stages of integration. The initial condition for the first phase is a stable pattern of mean temperature and salinity with no currents. The

model with 5 degrees in horizontal separations and 7 vertical layers was integrated for more than 40 years using 8-hour time steps until a quasi-equilibrium state was reached. Figure 4 shows the total kinetic energy fluctuation at the initial spin-up stage. After 10 years of integration, the local rate of change term was everywhere much smaller than other major terms in both the momentum and the thermohaline balance equations, as will be analyzed later. The results of the model output after 40 years of integration was interpolated to 2.5 degrees and 10 layers to be used as initial conditions for the second phase of the model. This version of the model was then integrated for more than 20 years until another quasi-equilibrium state was reached. Then the seasonally varying, time-dependent atmospheric conditions were imposed as upper boundary forcing conditions. The integration was carried out for another 20 years. The last year's output was considered as the long-term, seasonally varying state in the North Pacific Ocean. In the following papers (II and III), we will describe in detail the time-dependent, seasonal variability, and the anomaly experiments.

Energetic analysis under quasi-equilibrium state. The basic numerical scheme used in the model was emphasized the conservation of integral properties related to advection terms in both the momentum and the thermohaline equations. For each individual computational subvolume, balances of mass, momentum, heat, and water were properly taken into account. After a long period of time-integration, a quasi-steady state in the ocean was reached. We will discuss a few representative points of the North Pacific Ocean in depth to indicate the local dynamic balance of all forces involved in the system. Figure 5 shows the local balance of

all major physical processes included in the formulations, namely, the Coriolis term, the pressure gradient term, the horizontal and vertical viscous terms, and the horizontal and vertical nonlinear terms in the momentum equation of a subvolume near the western boundary region. Values indicating the relative magnitudes of each term in the momentum equation have been normalized in such a manner that the absolute sum of all terms is 100%. As shown in Figure 5a the dominating terms in the momentum balance are the Coriolis force, the pressure gradient force and the wind stresses in the surface layer. Since the x-component of wind stress is much stronger than the y-component, the surface current maintains an Ekman-geostrophic balance in the x-component of the momentum equations and in near geostrophic balance with high frictions for the y-component of the momentum equation. In the x-momentum equation near the surface within the Kuroshio region, the pressure gradient force and wind stress, having relative weights about 30% and 20%, respectively, balance the Coriolis force. It is expected that the nonlinear effect is relatively small, less than 1% in most places, as indicated in Figure 5 because of coarse grids in the model. The dominating flow in the Kuroshio region is northward and there exists a strong shearing in currents in the western boundary. As expected, the diffusive terms in the y-component of momentum equation contributes more than 10%, as shown in Figure 5c, which is much greater than that in the x-component. Figures 5b,d show the momentum balance in the lower layers of the ocean, at about 1000-m depth. It is obvious that the major terms are in geostrophic balance. The summation of all other terms contributes only less than 5%.

Similar conclusions have been shown by Bryan and Cox (1968) in the vorticity balance. Figure 6 shows the momentum balance near the equatorial region at 2.5°N, 165°W. The major forces are still in Ekman-geostrophic balance in the surface layer and in near geostrophic balance below, with the horizontal diffusion of momentum becoming increasingly important. In the x-component of momentum equation, the pressure gradient force, which is rather moderate in the longitudinal direction, works together with the Coriolis force of balance x-component of the surface wind stress, which is quite strong because of the trade wind. The horizontal diffusion of momentum as well as the nonlinear effect are becoming more important in the equatorial region. The former may account for up to 10% in the x-component and up to 20% in the y-component; and the latter may contribute up to 5% at some points (figures not shown). The nonlinear effect is small in most of the area in the ocean away from boundaries but is not negligibly small in the equatorial and in the western boundary regions. The y-component of momentum equation has a somewhat different balance. In the equatorial region, the y-component of Coriolis force is larger than the x-component because the equatorial currents flow mostly in the east-west direction. The north-south density gradient is larger than that in the east-west direction while the meridional component of the trades is much weaker than the zonal component. The balance is maintained between the Coriolis force, working together with the meridional wind stress and the pressure gradient force, assisted by the strong viscous effect. In the lower layers near the equator, the x-component of the viscous force becomes important due

mostly to large magnitudes and complicated patterns of the current system. The viscous force together with the Coriolis force balance the east-west pressure gradient force. The y-componant of momentum in the lower layers is generally in geostrophic balance as shown in Figure 6d. In the mid-latitude open ocean about 2000 km north-west of Hawaii in the Pacific wind drift current region, the Ekman dynamics is dominating in the x-component while the Ekman geostrophic balance is maintained in the y-component of momentum equations as shown in Figure 7. At the depth of intermediate water, there is essentially a geostrophic balance with most of other processes being negligibly small. In summary, below the surface layers geostrophy is the dominating balance in the present version of our model, while in the surface layer the Ekman drift together with associated convergence and divergence play an important role in the dynamic balance.

The scale analysis shows that in the density equation, consisting of both the temperature and the salinity equations, the advective terms are of the same order as other terms. It is interesting to note that, though the combined effect of the horizontal advection ($\nabla\cdot\vec{V}T$) and the vertical advection of heat ($\partial/\partial z(wT)$) (or salinity) is comparable to the diffusive terms, the magnitude of the individual term of the horizontal advection and the vertical advection of heat (or salinity) are much lager than other terms. Figures 8 and 9 show the thermodynamic balance in normalized relative weights in percentage at two representative subvolumes, one near the equatorial region (near 170°W) and the other in the mid-latitude open ocean. It shows clearly that the most dominating process for the local thermohaline

energy balance in the ocean is the advective terms. However, it seems always true that the horizontal advection terms and the vertical advection term are compensating each other as they are expected to be physically meaningful in the continuity requirement for incompessible fluid dynamics. Divergence (or convergence) will cause local surplus (or deficiency) of thermal energy which is invariably compensated by the deficiency (or surplus) as the result of upwelling (downwelling). Thus the consequential net effect of advective terms may still be as small as the other processes. This general tendency holds all over the ocean regardless of where the computational subvolume is. In considering the total balance, the surface heating turns out to be as important as the advection. The former may even be more important than the latter in the open-ocean region as indicated in Figure 8 where the current is relatively weak. From the figures we notice that a real steady state in the density distribution has not been reached though the salinity distribution is almost steady. The term analysis of salinity (figures not shown) shows the same relative weight distribution as that of the temperature distribution.

The above discussion leads to a concerned question to physical oceanographers who are seriously attempting to make in situ measurements of heat content in the ocean. Since the dominating influence in the local thermal energy equation is the surface heating from the atmosphere and the difference of two large advective terms, small errors in measurements will lead to a great uncertainty in the heat budget study. Acceptable accuracy may be obtained with modern instruments and technology

for the measurements of horizontal heat fluxes and surface heating. But, to my knowledge, the same accuracy for the measurement of vertical flux of heat is very difficult to obtain with the present level of oceanographic knowledge.

Annual long-term mean state. In the initial phase of integration, we used a 5-degree horizontal separation with 7 vertical layers, of which five were above 1000 m. Based on the internal gravity wave, the Courant-Fredericks-Lewy condition was satisfied in the coarse grid model by taking a time step of 8 hours. In the second phase of calculation, the model was refined to 2.5 degrees in the horizontal separations with 10 vertical layers, of which seven were above the main thermocline. A time step of 4.3 hours was taken. Parameters used in the 2.5-degree version of the model are summarized in Table 2. The baroclinic mode is predicted from the prognostic equations of shear currents and the barotropic mode is obtained from the stream function predicted by the vorticity equation. The temperature and salinity, hence the density, are obtained from predictive equations at all time steps. The only specified input to the model is the atmospheric state used in the surface boundary conditions.

Mass transport stream function. Figure 10 shows the contour plot of the mass transport stream function in a nearly equilibrium state under annual mean surface wind stresses and heating after more than 60 years of integration. Three large-scale gyral circulations are well developed, similar to the Munk solution (Munk, 1950). The anticyclonic subtropic gyre is quite realistically portrayed and the western intensification of the boundary current is clearly demonstrated. The major port of the

mid-latitude west drift current constitutes the northern portion of the subtropic gyre. The California Current, the North Equatorial Current as well as the Western Boundary Current are all included in this gyral current system. The maximum total transport in the Kuroshio region near Japan reaches 56 Sverdrups (56×10^6 m^3/sec) which agrees quantitatively with observed mean transport in the area (Nitani, 1972). Two cyclonic gyres are also well simulated, one of which is in the subartic region, the other in the tropic region. The subartic cyclonic gyre consists of the west drift current, the Alaskan Current, The Aleutian Current together with its extension through the Bering Sea, the Kamchatka Current, and the Oyashio Current. The mass transport of the model output in the Kamchatka Current region has a southward transport of 21 Sverdrups and in the Oyashio region, about 2 Sverdrups. Reid's (1973) analysis of the Boreas data indicates a geostrophic transport across 55°N relative to 1500 decibars of 23 Sverdrups in winter, while calculations made from summer data indicate only 8 Sverdrups (Allen, 1964). In the Oyashio region, Hata's (1965) data show a southward transport across 43°N of about 3 Sverdrups in winter and about 2 Sverdrups in spring and summer. Our model output agrees satisfactorily with observed data. However, the simplification of configurations in the model has ignored the existences of islands, including the Aleutian chain of islands, and resulted the disappearance of many interesting small-scale features in the circulation pattern. We notice that the Aleutian stream is absent in the stream function and the Alaskan gyre is flowing to the west instead of to the southwest. The mass transport in the tropic cyclonic gyre with the annual

mean atmospheric forcing reaches a maximum value of 25 Sverdrups. The gross feature of the stream function patterns shows similar distribution to that of the wind stress curl. Transports in the boundary regions between the cyclonic and the anitocyclonic gyral circulations are weak, in coincidence with the latitude of zero curl regions and the maximum transport occur at corresponding maximum wind stress curl latitudes as pointed out by Munk (1950). The barotropic current deduced from the stream function is generally small, less than 1 cm/sec everywhere in the basin except in the western boundary region.

Note in Figure 10 there are slightly wavy streamlines in the mid-latitude region near Japan. This is probably because the eddy viscosity used is still too small for this coarse grid (Takano, 1976).

Velocity patterns. Figures 11a,b,c show current vector plots for the layers at a depth of 10 m, 250 m, and 2500 m, respectively. Figures 12a,b,c show streamline plots for these same levels. In the surface layer the major swift currents occur in the equatorial region as well as in the western boundary region. The maximum current is shown in the eastern central Pacafic near the equator with a speed of 95 cm/sec. The Kuroshio Current only reaches 64 cm/sec due mostly to the coarse grid meshes. We notice that the western boundary current is only barely resolved at the horizontal separation of about 175 km. The nondimensional length scale for a frictional western boundary, L_F, is proportional to the one-third power of the Ekman number ($E = \nu_1/2\Omega a^2$ and $L_F = E^{1/3}$). The value of L_F for the second phase is 0.012. The resolvable length scale for the Kuroshio Current is 340 km during the second stage of computations. It is

obvious that the grid separation is just barely comparable with the observational width of the western boundary current. Thus, the coarse grid separations have led to smaller current values than the observations, while the transport values and comparable. The scale width of the inertial boundary layer, L_I, is proportional to the square root of the Rossby number ($L_I = Ro^{1/2}$). The nonlinear effects were included in the model with $L_I = 0.0045$. After comparing L_F with L_I, it is evident that the inertial effects are smaller than the viscous effects, however, they are not negligible, as ascertained in the previous momentum analyses. The surface currents in the tropics are generally flowing westward. The equatorial countercurrent is not clearly shown, most probably due to the coarse grid. The Oyashio merges into the extension of the Kuroshio to form the North Pacific drifting current. The streamline plot for the surface layer is shown in Figure 12a. It is evident that the surface current is dominated by the wind pattern. In the equatorial region, the flow pattern splits into a northward branch to form the Kuroshio and a southward branch of the equatorial current system near the Phillipine Sea. The existence of the subartic convergence zone is clearly shown along the mean track of the Kuroshio and Oyashio merging zone off the western boundary at about 40°N, leaning southward to the eastern North Pacific at about 35°N. A mesoscale anticyclonic eddy, recognized as the Eastern Gyral by Sverdrup (Sverdrup, et al., 1942) exists in the mid-latitude eastern North Pacific. Figures 11b and 12b show the current vector and the streamline plot of the layer at 250-m depth. Notice that the current near the equatorial region is flowing eastward, representing the combined flow of the north

equatorial countercurrent and the Cromwell undercurrent. The Kuroshio is well developed and has the maximum velocity of 35 cm/sec, the highest value in the layer. The 250-m gyre picture looks very much like transport maps of White (1975). Note that the surface convergence line exists at the center of the geostrophic gyre at 250 m and that the eastern surface gyre does not show up at depth. The Kuroshio Current, the west wind drift, the California Current, and the North Equatorial Current are predominently and easily identified with the anticyclonic gyre. The tropic cyclonic gyre consisting of the North Equatorial Current, the equatorial countercurrent together with the equatorial undercurrent, is clearly demonstrated. Other less obvious currents, such as the Oyashio and the Alaska Currents, are indicated in the circulation pattern. Figures 11a,b and 12a,b simulate the gross nature of the circulation patterns in the upper layers of the North Pacific Ocean as, for example, shown in Figure 13 which indicates the surface mean current in more detail. The simulated current near 700 m is rather weak and the circulation indicates a different pattern (figure not shown). In the deep layers currents are slightly stronger than in layer 7 and the circulation pattern below the depth of 1500 m, as shown in Figures 11c and 12c, is opposite to that of the upper layers. The current beneath the Kuroshio is flowing southward at a much slower speed of 4 cm/sec and there is clearly a weak cyclonic circulation in the subtropic region. Deep water is slowly flowing southward from the high latitudes in the western North Pacific and northward in the eastern North Pacific, and that generally agrees with the deep circulation pattern deduced from the geostrophic calculation

of Reid (1976, personal communication).

Figure 14 shows the vertical velocity contours at the bottoms of aforementioned three layers (i.e., at 20 m, 300 m, and 2200 m depths, respectively) in the model ocean. The solid contour indicates upwelling and the dotted line, downwelling. There are, in general, strong upwellings along the equator, especially in the eastern part of the mid-tropic region where the maximum upwelling reaches 5 m/day. Upwellings in the mid-latitude, western boundary region are relatively weak in the surface layer. There also exist weak upwellings along the California coast. Weak downdwellings exist in most subtropic and eastern tropic regions away from the equator. This pattern of equatorial upwellings and subtropic downdwellings extends to a depth of more than 700 m. In deeper layers, upwellings along the western boundary and downwellings in the high latitudes and in the north-western part of the North Pacific become even stronger at the depth of 1500 m. The maximum upwelling reached 3.5 m/day in the western boundary at a depth of 200 m and the maximum downwelling of approximately 1 m/day at the high latitude region occurred at a depth of 550 m. The equatorial upwelling decreases below 200 m and a slight upwelling was indicated in the tropics at the 1000-m depth. However, below 1000 m, the general trend of upwelling and downwellings generally changed signs. There exist moderate downwellings in the western boundary at 1000 m and weak upwellings in the high latitudes. At the depth of 2500 m, weak upwellings become evident in most of the northern boundaries and moderate downwellings exist in the equatorial region. There are weak but broad upwellings in the interior of the tropics. From the previous

figures we notice that major large-scale features in the model match nicely with observed mean current patterns and upwelling distributions in the North Pacific Ocean.

Density field. Density is a diagnostic parameter obtained from the temperature and salinity according to the equation of state. Several formulations based on empirical data are available (e.g., Eckart, 1958; Bryan and Cox, 1970; Friederick and Levitus, 1970). In the present run the simplest form was used,

$$\rho = \rho_o[1-\alpha(T-To) + \gamma(S-So)] \qquad (76)$$

where values of To, So, α, and γ are chosen from appropriate data as shown in Table 2. Since both T and S are prognostic variables in the model, we have examined the temperature and salinity field instead of the density field. Figure 15 shows the temperature patterns at depths of 10 m, 250 m, and 3000 m, respectively. The surface temperature distribution (Figure 15a) shows an equatorial cool region extending from the east boundary to 180°, corresponding to the equatorial upwelling region. The broadest cold water extends to 5°N with a minimum of 23°C at the equator. There is a broad warm water region in the western tropic and a narrow one near the eastern boundary north of the equator. A sharp meridional temperature gradient exists in the mid-latitude off the western boundary along 35°N. The upwelling along the equator does not penetrate deeply around 300 m, warm water masses in the western and eastern tropics can still clearly be discerned and a sharp temperature gradient along the western boundary develops. At 1000 m (figure not shown), the temperature

is quasi-homogeneous and is slightly warm in the south. The deep water at 3000 m shown in Figure 15c indicates a spatial homogeneity with a slight cooling in the north. Because of our limited knowledge concerning the interior of the ocean, verifications for the model ouput are rather difficult. Nevertheless, certain climatological atlases are available for comparisons. In general, the distribution agrees well with the mean sea surface temperature pattern in the North Pacific Ocean as shown in Figure 16 (Masuzawa, 1972). In the mid-latitude and tropic regions, the agreement between Figures 15a and 16 is very good. However, a close examination reveals that the observed winter temperature at high latitudes is slightly lower than the model temperature, which is much closer to the summer values (Figure 16a). Since the temperature changes depend mostly on the constrained atmospheric conditions, especially the air temperature, the annual mean atmospheric data used in the model as upper boundary conditions is probably biased to the summer conditions mostly because ther were more observations during the summer season. The similar temperature patterns extend down below to 100 m with a slight overall decrease of about 2°C at the 60-m depth and about 7°C at the 100-m depth, except the cool water along the equator, that has been narrowed to 1 or 2 degrees in latitude at the 60-m depth and disappeared at 100 m.

Temperature distributions for longitudinal vertical cross sections at 5°N, 15°N, 25°N, and 35°N are shown in Figure 17. There is always a sharp vertical temperature gradient about 0.5°C/m above the main thermocline, which is about 300 m in the tropics. It is about 0.015°C/m in the intermediate water from the main thermocline down to the depth of 1000 m.

The temperature is rather homogeneous with a weak vertical gradient about 0.0007 °C/m below the depth of 1000 m. Water is generally warm in the west North Pacific (32°C to 34°C), cool in the middle-east North Pacific (about 24°C to 25°C), and becomes warm again near the eastern boundary (about 29°C to 30°C) in the surface layer at 5°N near the topics. The eastern warm mass extends westward to 135°N and more. The surface mixed layer is about 50 m to 100 m deep in the mid-latitude as shown in Figure 17d. The observed corresponding temperature distributions in the longitudinal cross sections of Figure 17 are shown in Figure 18, obtained from Moromtsev (1963) and from Masuzawa (1972). The general feature of the model output agrees qualitatively well with observed and atlas data. The same order of magnitude of vertical temperature gradients exists in the upper 350 m. However, there are no spatially wavy distributions of temperature and no double thermoclines in the simulated temperature field as have been shown in the atlas. This is probably due to the coarse vertical separations in the model. The model of the eastern North Pacific produced more warm water in the middle latitude, where the isotherms rise very gently to the east in the intermediate water depth (300 m to 700 m), as indicated in Figures 17c,d, than that of the atlas where the isotherms rise rather sharply toward the east as shown in Figures 18c,d.

Four meridional cross sections of temperature distribution of the model output are shown in Figure 19 and four corresponding cross sections of oceanographic surveyed profiles are shown in Figure 20. The gross features of the two figures bear general agreement, except the isotherms in

the model output are much smoother than the observed ones. The major discrepancy occurs in the high latitude region above 45°N where the simulated temperature is warmer. The 4°C isotherm never reaches the surface in the model as it does in the observed data. This is mostly caused by the annual mean atmospheric forcing conditions which are biased by northern summer observations. Warm air temperatures in high latitudes used as constrained boundary conditions result in a correspondingly warm oceanic temperature distribution in the subartic region. The overadjustment of the convective mechanism in the unstable water column also affects the mixed layer depth which is rather deep in the model.

Simulated salinity distributions for three layers at surface, 350 m, and near the bottom (3000 m) are shown in Figures 21a,b,c, respectively. The surface salinity shows an elongated maximum zone above 35°/oo between 20°N and 30°N and declines polarward and equatorward as indicated in Figure 21a. In the eastern tropic, there is also a high salinity tongue near the boundary and extending westward. The north-south homogeneity is indicated in the western boundary region. At the depth of intermediate water level, salinity values are slightly higher, around 34.4°/oo to 35.2°/oo, than that of the surface layer but with similar patterns as shown in Figure 21b. The salinity in the bottom water is rather homogeneous with a slight high in the northwest. Reid's (1969) surface salinity distributions are shown in Figure 22. General agreements in large-scale features between Figures 21a and 22 are satisfactory. Three meridional vertical cross sections at 180°, 105°W, and 165°E are shown in Figures 23a,b,c, respectively, for the simulation and in Figures 24a,b,c,

for the observed atlas data (Moromtzev, 1963). The gross nature in the corresponding cross sections in Figure 23 and Figure 24 agrees qualitatively well. In the western North Pacific along 105°W, a maximum near 20°N and a minimum near 5°N are shown in Figures 23a and 24a. Along the 180° cross section, a large amount of low-salinity but high-density water sinking near 40°N to an intermediate water depth around 500 m to 1000 m is clearly indicated in both Figures 23b and 24b. There is a shallow salinity minimum in the vertical at the depth around 100 m, a maximum at the depth around 300 m and a prominent minimum at the intermediate water depth. These features are also clearly shown in the eastern central North Pacific in both Figures 23c and 24c. Certain discrepancies do exist between the simulated and the observed salinity distributions. The simulated salinity in the high-latitude region north of 40°N is about 1°/oo higher than atlas data and the maximum salinity zone is closer to the eastern boundary than is the observed one. This is mostly caused by the inaccuracy of the evaporation and precipitation data imposed as the upper boundary condition. These data were obained from Jacobs (1951). Recent studies (e.g., Reed and Elliot, 1973) have indicated that much high precipitation occurs in the subartic region.

Pressure field and dynamic topography. The surface pressure can be calculated explicitly from the vertically integrated momentum equations,

$$\left(\frac{p_o}{\rho_o}\right)_\lambda = \psi_{\varphi t}\cos\varphi + f\psi_\lambda - a\hat{G}\cos\varphi - \frac{g}{\rho_o D}\int_{-D}^{0}\int_{z}^{0}\rho_\lambda dz'dz + a\hat{F}^\lambda\cos\varphi \qquad (77)$$

$$\left(\frac{p_o}{\rho_o}\right)_\varphi = \psi_{\lambda t}\sec\varphi - f\psi_\varphi - a\hat{G}^\phi - \frac{g}{\rho_o D}\int_{-D}^{0}\int_{z}^{0}\rho_\varphi dz'dz + a\hat{F}^\phi \qquad (78)$$

where p_o is the surface pressure, ψ is the stream function defined in (31) and (32). F and G are defined in (9), (10), (34, (35). The p_o can be obtained by integrations with an arbitrary constant appropriately adjusted with a known pressure point. Then the pressure at all depths can be found by integrating the hydrostatic Eq. (29). The surface barotropic pressure above the balanced level surface can be approximated, excluding the very small surface baroclinic and kinematic effects, as

$$p_o = p_a + \rho_o g\eta \tag{79}$$

where η is the surface elevation and p_a is the atmospheric surface pressure.

The pressure field at the surface (10 m) and at the depths of 225 m and 3000 m are shown in Figure 25 in units of 0.1 m^2/sec^2. The pressure field, Figure 25a, shows sharp horizontal gradients in the Kuroshio region, indicating a strong northward current. The pressure gradients outside of the boundary indicate a broad eastward flow in the mid-latitudes and a weak south-westward flow in the tropics. At the depth of 225 m, the basic pattern of surface flow still exists at this depth except with more northward flow in the subartic and more westward flow in the tropics. Near the bottom layer at a depth of 3000 m, the geostrophic circulation is opposite of that in the upper layers. There is southward flow beneath the Kuroshio Current and a broad westward flow under the North Equator Current.

The dynamic topography of the sea surface based on observational density field with respect to a 1000-db is shown by Wyrtki (1974) and the

mean dynamic height in the North Pacific Ocean is reproduced as shown in Figure 26. Though detailed information is not portrayed in the computed pressure field, especially near the equator, general features of the surface pressure, Figure 25a as the relative field of the surface elevation compares very favorably with annual mean dynamic topography in the North Pacific as shown in Figure 26. Note that the dynamic height in Figure 26 corresponds to the surface pressure values in Figure 25 divided by the gravitational acceleration, and the difference is just an arbitrary integration constant.

Energetics. The energy conservation for the model has been discussed briefly in the last paragraph of the formulation. The rate of change of kinetic energy per unit volume can be expressed symbolically as

$$K_t = K'_t + \bar{K}_t = \langle G \rangle + \langle p\sim K \rangle + \langle \tau \rangle + \langle DV \rangle + \langle DW \rangle \qquad (80)$$

where $\bar{K}$ and K' are the rate of change of vertical mean and deviation from the mean kinetic energy per unit volume; G denotes the nonlinear effect; $(p\sim K)$, the transformation between the potential energy and the kinetic energy due to buoyant effect; τ, the work done on the surface of the ocean by wind stress; (DV), the dissipation of kinetic energy due to horizontal eddy viscosity; and (DW), the dissipation of kinetic energy due to vertical eddy viscosity. The rate of change of potential energy per unit volume can be expressed as

$$P_t = \langle GP \rangle - \langle p\sim K \rangle + \langle DP \rangle \qquad (81)$$

where $P = \rho g(z+D)$ is the potential energy defined as before; (GP) denotes the advection of potential energy; (p~K) the conversion of potential energy to kinetic energy or vice versa; and (DP), the diffusion of potential energy including all thermocline sources and sinks. Note that if integration is carried out for the whole mechanically closed domain, the advection effects such as G and (GP) contribute no work. However, redistribution of kinetic energy between the baroclinic mode K' and the barotropic mode $\bar{K}$ does happen because of the nonlinearity. Note also that the conversion between the potential and the kinetic energy occurs only in the baroclinic mode because the ocean bottom is flat in the present study (Wiin-Nielsen, 1962; Holland, 1973).

The energetic diagram showing the magnitude and direction of work done per unit volume in ergs cm^{-1} day^{-1}, together with the total potential and the total barotropic and baroclinic energy in erg/cm^3 are shown in Figure 27. Potential energy is computed with reference to the ocean bottom. It is clear from Figure 27 that the kinetic energy, from both the barotropic and the baroclinic modes, has reached a steady state but the potential energy is still losing energy at a rate of 2.5 $ergs/cm^3/day$. In the North Pacific model, a major portion of the surface area is in the tropic and subtropic region. This leads to a relatively large amount of input heat and output evaporation across the ocean surface as a whole. These net thermal and haline effects dominate the equilibrium potential energy state, the former decreases the potential energy while the latter increases it. As shown in the energy diagram, the thermal effect is very influential. A small portion of potential

energy is increased due to the net upwelling induced by the mechanical input of wind stresses. As pointed out by Haney (1974), consistent with Holland's (1972) result, the energy transformation is from the kinetic to the potential energy when the thermal boundary layer is greater than the viscous boundary layer as it is in the case of the present model, based on scale considerations. The diffusive effects also act on the positive side of the potential energy. Since the model has reached a quasi-equilibrium state, the energy loss due to the convective adjustments under unstable conditions is small. The kinetic energy is derived from the surface wind. Most of the mechanical energy input goes to the baroclinic mode. There is a small amount of energy conversion between the baroclinic mode and the barotropic mode due to the nonlinear effect.

Energy transport. One interesting and important problem in the numerical ocean simulation is to find out how much energy is transported by the ocean in the atmosphere/ocean system. In general, thermal energy must be transported poleward from low latitudes to high latitudes. The total northward transport of heat across a latitudinal circle in the ocean domain can be expressed as

$$H_T = \rho_o C_p \int_{-D}^{0} \int_{\lambda_o}^{\lambda_I} \left[(\hat{v}+v')\, T - \kappa_1 \frac{\partial T}{a\partial\varphi} \right] a\cos\varphi d\lambda dz \qquad (82)$$

where terms in the square bracket are the barotropic and baroclinic part of the meridional velocity and the north-south diffusion due to temperature gradient and λ_o and λ_I are the longitudes of the western and the eastern boundaries, respectively. The results are shown in Figure 28. Most of the poleward thermal energy in the tropic and subtropic region

is transported by the baroclinic advection (Hv') which has approximately the same magnitude as the energy flux transported by the total current (Hv). The diffusion of heat (Hd) contributes relatively little in the low and high latitudes and is equatorward in the tropics. However, in the mid-latitude region where the meridional temperature gradient is large and the current is mostly zonal, the transport of heat energy by diffusive processes is important. The total rate of the northward thermal energy transport is about 2×10^{14} cal/sec. Maximum transports occur at latitudes between 20°N and 35°N.

Since the poleward energy transport by ocean currents is important in the dynamics of climate fluctuations, it has been studied for many years by many scientists (e.g., Jung, 1952; Sverdrup, 1957; Budyko, 1958; Albrecht, 1960; Bryan, 1962). Vonder-Haar and Oort (1973) have made a new estimate of the annual poleward energy transport based on recent measurements of the earth's radiation budget from satellites, together with atmospheric energy transport summaries based on rawinsonde data. Their results are shown in Figure 29. The peak oceanic heat transport (2.5×10^{22} cal/year) occurs near 20°N and accounts for 74% of the energy transport at that latitude. On the average, the ocean contributes about 40% in the northern hemisphere for the required energy in the atmosphere/ocean/earth system. Sellers' (1965) estimation based on the surface energy budget of Budyko (1963) is also shown in Figure 29, as BS. As pointed out by Vonder-Haar and Oort, Sellers' estimation is relatively lower. The computed energy transport in the North Pacific Ocean model, indicated as NPO, is also shown in Figure 29. Though quantitative comparison between

the observational estimates and the model output without the energy transport from the Atlantic and the Indian Ocean is not meaningful, it is certain that the total simulated oceanic energy transport including the above-mentioned transports would be closer to the recent estimate by Vonder-Haar and Oort (1973).

5. Summary and conclusions

Based on Haney's (1974) idealized basin model, a North Pacific Ocean model has been developed for the study of the physical nature and dynamic behaviors of large-scale, long-term fluctuations in the North Pacific Ocean. During the first stage of time integration, a coarse grid mesh with horizontal separation of 5 degrees and 7 layers, was used to obtain the long-term mean state of the circulation. In the second stage, the model was refined to 2.5 degrees in horizontal separations with 10 layers in vertical. Annual mean observed atmospheric data were imposed as the upper boundary conditions. After about 60 years of integration in the second phase, a quasi-equilibrium state in the ocean was reached and the time-dependent, seasonal atmospheric conditions were imposed to obtain seasonal responses and time-dependent variations in the ocean. Another 20 years or more integration was carried out and daily values of the last years were used as the mean seasonal state. Prediction experiments were carried out using the observed anomalies together with the mean seasonal state in the ocean for the understanding of the dynamics involved in the generation, propagation, evolution, and dissipation of thermal anomalies which were observed in the North Pacific Ocean. The present paper deals with the long-term mean state in the completion of the second phase.

Dynamic analyses show that geostrophic balance is approximately maintained all over the ocean in the lower layers. In the surface layer, the momentum balances are in general between the Coriolis force and the surface stress in the zonal equation and between the Coriolis force, the

surface stress, and the pressure gradient force in the meridional equation. Internal vertical eddy viscosity contributes about 10% to the balance. The nonlinear terms are generally small but not negligible. In the heat and salinity equations, the convergency of the advective fluxes of heat and salinity are the dominating terms. This leads to the question as to how accurately the energy budget in a measurable volume of water in the real ocean can be calculated. Since the horizontal and vertical fluxes tend to balance, small errors involved in the measurement of the transports, especially the vertical one, may result in large residual errors in the heat budget.

The vertically integrated stream function shows three gyre circulators in the North Pacific Ocean, one anticyclonic gyre in the subtropic, and two cyclonic gyres in the tropic and subartic regions, respectively, similar to the solutions of a diffusive ocean (Munk, 1950). Layer-by-layer velocity patterns show surface flow toward the west and deep flow toward the east near the equator, indicating the simulation of the South Equatorial Current and the Cromwell Current. There is a northward Kuroshio Current above 700 m and a returning southward flow underneath it. The layer-by-layer streamline patterns show large-scale anticyclonic circulations above 1000 m and opposite patterns below. There are strong upwellings near the equator and at the western boundary in the upper two layers and downwellings in the lower layers in the equatorial region. The simulated gross nature of temperature and salinity distributions compare well with observed field atlas data. The surface pressure field also compares satisfactorily with dynamic height distribution based on density

observations. The northward transport of thermal energy is accomplished mostly by the baroclinic current and the total thermal energy transport is rather large (1.1×10^{22} cal/year). However, both temperature and salinity values from the model are higher than observed mean data in high latitude. This is mostly due to the higher annual mean air temperature and lower evaporation and precipitation values imposed upon the model than these in the real atmospheric field.

The present regional North Pacific model demonstrated its ability to portray the large-scale mean circulation patterns and mean density field in the North Pacific. The major objective of performing the anomaly prediction experiments for the understanding of anomaly dynamics in the ocean justifies the step-by-step approach to obtain the time-dependent, long-term mean ocanic state. A series of numerical studies, imposing anomalous heat fluxes and varying wind stresses as well as the anomalous initial state in the ocean have been carried out. The follow-up papers, II and III, will deal with time-dependent oceanic state's and anomaly experiments.

Acknowledgments

I wish to express my sincere thanks to the following individuals for their encouragements, discussions, and assistances: Professor J. D. Isaacs and Dr. J. Namias for encouragements and discussions; Drs. K. Bryan and R. L. Haney for providing their early models and also Dr. R. L. Haney for providing the atmospheric forcing data and for many spirited discussions; Drs. W. L. Gates, J. J. O'Brien, W. R. Holland, R. C. Allexander, and Warren B. White for instrumental discussions and for comments on the manuscript; to Drs. W. Y. Shaw, J. M. Park, and R. A. Wylie for certain portions of programming and presentation assistance.

Most of the computer resources for this study were provided by the National Center for Atmospheric Research, which is sponsored by the National Science Foundation. This research was supported by the National Science Foundation and the Office of Naval Research under the North Pacific Experiment of the International Decade of Ocean Exploration. These supports are gratefully acknowledged.

References

Albrecht, F., 1960: Jahreskarten des Warme-und Wasserhaushaltes der Ozeane. (Annual charts of the heat and water balance of the oceans.) Ber. Deut. Wetter., Germany, 9, 66, 3-19.

Allen, J., 1964: A description report on the physical and chemicical properties of the north-western Pacific Ocean during summer 1963. U.S. Naval Oceanogr. Off. No. O-17-64.

Arkawa, A., 1966: Computational design for long-term numerical integration of the equations of fluid motion: two-dimensional incompressible flow, Part I. J. Comput. Phys., 1(1), 119-143.

Arthur, R. S., 1966: Estimation of mean monthly anomalies of sea-surface temperature. J. Geophys. Res., 71(10), 2689-2690.

Bjerknes, J., 1962: Synoptic survey of the interaction of sea and atmosphere in the North Atlantic. Geofys. Publik., Oslo, 24(3), 11-145.

____, 1966: A possible response of the atmospheric Hadley circulation to equatorial anomalies of ocean temperature. Tellus, 19(4):830-829.

_____, 1969: Atmosphere teleconnections from the equatorial Pacific. Mon. Wea. Rev., 47(3), 162-172.

_____, 1972: Large-scale atmospheric response to the 1964 Pacific equatorial warming. J. Phys. Oceanogr., 2, 212-217.

Bryan, K., 1962: Measurements of meridional heat transport by ocean currents. J. Geophys. Res., 67, 9, 3403-3414.

_____, 1963. A numerical investigation of a nonlinear model of a wind-driven ocean. J. Atmos. Sci., 20, 594-606.

Bryan, K., 1969a: Climate and the ocean circulation: III, the ocean model. Mon. Wea. Rev., 97(11), 806-827.

_____, 1969b: A numerical method for the study of the circulation of the world ocean. J. Comput. Phys., 4(3), 347-376.

_____, and M. D. Cox, 1967: A numerical investigation of the oceanic general circulation. Tellus, 19(1), 54-80.

_____, and _____, 1968. A nonlinear model of an ocean driven by wind and differential heating: Part I and part II. J. Atmos. Sci., 25, 6, 945-978.

_____, and _____, 1970: An approximate equation of state for numerical models of ocean circulation. J. Phys. Oceanogr., 2,

_____, and _____, 1972: The circulation of the world ocean: a numerical study. Part I, a homogeneous model. J. Phys. Oceanogr., 2, 319-335.

Budyko, M. I., 1958: The heat balance of the earth's surface. (Teplovoi balans zemnoi poverkhosli, 1956), N. A. Stepanova, translator, U.S. Weather Bureau, Washington, D.C., 259 pp.

_____, 1963: Atlas of the heat balance of the globe (in Russian). Moscow, Hydrometeorological Service, 69 pp.

Bussinger, J. A., J. C. Wyngaard, Y. Izumi and E. F. Bradley, 1971: Flux-profile relationships in the atmospheric surface layer. J. Atmos. Sci., 28, 181-189.

Bye, J.A.T., and T. W. Sag, 1972. A numerical model for circulation in a homogeneous world ocean. J. Phys. Oceanogr., 2(4),

Cox, Michard E., 1970: A mathematical model of the Indian Oean. Deep-Sea Res., 17(1), 47-75.

Crowley, W. P., 1968: A global numerical ocean: Part I. J. Comput. Phys., 3, 111.

_____, 1970: A numerical model for viscous, free-surface barotropic wind driven ocean circulation. J. Comput. Phys., 5, 139-168.

Deerdorff, J. W., 1968: Dependence of air-sea transfer coefficients on bulk stability. J. Geophys. Res., 73, 8, 2549-2557.

Eckart, C., 1958: Properties of water, Part III. Am. J. Sci., 256, 255-240.

_____, 1960: Hydrodynamics of Ocean and Atmosphere. Pergamon Press, New York, 290 pp.

Freiderick, H., and S. Levitus, 1970: An approximation to the equatorial state for sea water suitable for numerical ocean model. J. Phys. Oceanogr., 2,

Gates, W. W., E. S. Batten, A. B. Kahle and A. B. Nelson, 1971: A documentation of the Mintz-Arakawa two-level atmospheric general circulation model. Adv. Res. Proj. Agency, R-877-ARPA.

Gormatyuk, Yu.K., and A. W. Sarkisyan, 1965: Results of four-level model calculations of North Atlantic currents. Izv., Atmos. Oceanic Phys. Ser., 1(3), 313-326.

Haney, R. L., 1974: A numerical study of the response of an idealized ocean to large scale surface heat and momentum flux. J. Phys. Oceanogr., 4, 145-167.

Hata, K., 1965: Seasonal variation of the volume transport in the Oyashio area. J. Oceanogr. Soc. Japan, 21, 193-201.

Hess, S. L., 1959: Introduction to Theoretical Meteorology. Holt, Rinehart and Winston, New York, 355 pp.

Holland, W. R., 1967: On the wind driven circulation in an ocean with bottom topography. Tellus, 19(4), 582-599.

_____, 1972: Energetics of baroclinic oceans. Paper presented at the Symposium on Numerical Models of the Ocean Circulation. Durham, New Hampshire, October 17-20.

_____, 1973. Baroclinic and topographic influences on the transport in western boundary currents. Geophys. Fluid Dyn., 4, 187-210.

_____, and A. L. Hirschman, 1972: A vertical calculation of the circulation in the North Atlantic Ocean. J. Phys. Oceanogr., 2, 336-354.

Huang, J.C.K., 1973. A multi-layer, nonlinear regional dynamic model of the North Pacific Ocean. Scripps Inst. Oceanogr. Sc. ref. 73-23.

Il'in, A. M., V. M. Kamenkovich, R. G. Zhugvina and M. M. Silkina, 1969: On the calculation of complete circulation in the world ocean. Izv.: Atmos. Oceanic Phys., 5, 1160-1171.

Isaacs, J. D., 1968: Probing the birthplace of American weather. Naval Research Reviews, Office of Naval Research, Washington D.C., 13 pp.

Jabobs, W. C., 1951: The energy exchange between sea and atmosphere and some of its consequences. Bull., S.I.O., 6(2), 27-122.

_____, 1967: Numerical semiprediction of monthly mean sea-surface temperature. J. Geophys. Res., 72(6), 1681-1689.

Johnson, T. H., G. A. Flittner and M. W. Cline, 1958: Automatic data processing program for marine synoptic radio weather reports. Special Scientific Report 503, Bureau of Commercial Fisheries, 74 pp.

Jung, G. H., 1952: Note on the meridional transport of energy by the oceans. J. Marine Res., Sears Foundation, 11, 2, 639-649.

Lilly, D. K., 1965: On the computational stability of numerical solutions of time-dependent nonlinear geophysical fluid dynamics problems. Mon. Wea. Rev., 93, 1, 11-26.

London, J., 1957: A study of the atmospheric heat balance. Final report No. AF19(122)-165. Department of Meteorology and Oceanography, New York University, 99 pp.

Manabe, S., 1969: Numerical integrations of the primitive equations by a simulated backward difference method. J. Meteorol. Soc. Japan, Ser. 2, 44, 76-84.

Massuzawa, J., 1972: Water characteristics of the North Pacific central region. (Chap. 4 of Kuroshio, ed. by Stommel, H. and K. Yoshia. University of Washington Press.)

Matsuno, T., 1966: Numerical integrations of the primitive equations by a simulated backward difference method. J. Meteorol. Soc. Japan, Ser. 2, 44, 76-84.

Moromtsev, A., 1963: The principal hydrological features of the Pacific Ocean. GIMIZ, Leningrad, 417 pp.

Munk, W. H., 1950: On the wind-driven ocean circulation. J. Met., 7(2), 79-93.

Namias, J., 1959: Recent seasonal interactions between North Pacific water and the overlying atmosphere condition. J. Geophy. Res., 64(6): 631-646.

Namias, J., 1965: Macroscopic association between mean monthly sea-surface temperature and the overlying winds. J. Geophys. Res., 70(10), 2307-2318.

_____, 1969: Seasonal interaction between the North Pacific Ocean and the atmosphere during the 1960's. Mon. Wea. Rev., 97(3), 173-192.

_____, 1970: Macroscale variations in sea-surface temperature in the North Pacific. J. Geophys. Res., 75(3), 565-582.

Nitani, H., 1972: Beginning of the Kuroshio. In the Kuroshio Chap. 5, ed. H. Stommel and K. Yoshida, pp. 129-163.

O'Brien, James J., 1971: A two-dimensional model of the wind-driven North Pacific. Invest. Pesquera, 35(1),

Petterssen, S., D. L. Bradbury and K. Pedersen, 1962: The Norwegian cyclone models in relation to heat and cold sources. Geofys. Publik., Oslo, 24(9), 243-280.

Reed, R. K., and W. P. Elliot, 1973: Precipitation of ocean weather stations in the North Pacific. J. Geophys. Res., 78, 30, 7087-7091.

Reid, J. L., 1969: Sea surface temperature salinity and density of the Pacific Ocean in summer and winter. Deep-Sea Res., Suppl. to Vol. 16, 215-224.

_____, J. L., 1973: North-west Pacific Ocean water in winter. The Johns Hopkins University Press, 96 pp.

Rodewald, M., 1963: Sea-surface temperature of the North Atlantic Ocean during the decade 1951-1960, their anomalies and development in relation to the atmosphere circulation. Arid Zone Res., 20, 97-107.

Schulman, E. E., and P. P. Niller, 1970: Topographic effect on the wind-driven ocean circulation. Geophys. Fluid Dyn., (1), 439-462.

Sellers, W. D., 1965: Physical climatology. University of Chicago Press, 272 pp.

Sverdrup, H. U., M. W. Johnson and R. H. Fleming, 1942: The Oceans, Their Physics, Chemistry and General Biology. Prentice-Hall, Inc., New Jersey, 1087 pp. (in p. 723).

_____, 1957: Oceanography. Handbuch der Pitysik, 48, Akademe-Verlag, Berlin, pp. 608-670.

Takano, K., 1969: General circulation in the global ocean. J. Oceanogr. Soc. Japan, 25, 48-50.

_____, 1976: Eddy viscosity and grid size in ocean models. J. Oceanogr. Soc. Japan (in press).

Vonder-Haar, T. H., and K. J. Hanson, 1969: Absorption of solar radiation in typical regions. J. Atmos. Sci., 28, 4, 652-655.

_____, and A. H. Oort, 1973: New estimate of annual poleward energy transport by northern hemisphere oceans. J. Phys. Oceanogr., 3, 2.

Warren, B. A., 1963: Topographical influence in the path of the Gulf Stream. Tellus, 15(2), 167-183.

Wiin-Nielson, A., 1962: On transformation of kinetic energy between the vertical shear flow and the vertical mean flow in the atmosphere. Mon. Wea. Rev., 90, 311-323.

Wyrtki, K., 1974: The dynamic topography of the Pacific Ocean and its fluctuations. Hawaii Inst. Geophys., HIG-74-5.

White, W. B., 1975: Secular variability in the large-scale baroclinic transport of the North Pacific from 1950 to 1970. J. Marine Res. (33), 141-145.

Table 1

Description of symbols in ocean model

t	time
λ	longitude
φ	latitude
z	height
Ω	angular speed of the earth
a	radius of the earth
g	acceleration of gravity
u	zonal component of the current
v	meridional component of the current
V	reference horizontal velocity
w	vertical component of the current
T	temperature
S	salinity
ρ	density
F^{λ}	eastward frictional force per unit volume
F^{φ}	northward frictional force per unit volume
∇	horizontal gradient operator
h	step function incorporated with density stability
G^{λ}	nonlinear component in the zonal direction
G^{φ}	nonlinear component in the meridional direction
Q_S	downward heat flux
Q_I	incoming solar radiation

Table 1 (concluded)

Q_B	back radiation
Q_H	sensible heat
Q_E	latent heat
Q_o	incoming solar radiation with a clear sky
N_c	cloudiness in tenths
e_a	vapor pressure of air
e_s	saturated vapor pressure
T_s	ocean surface temperature
T_a	air temperature
c	Stefan-Boltzmann constant
L	latent heat of evaporation
ρ_a	air density
V_a	wind velocity
q	specific humidity
P_a	air pressure
C_D, C_E, C_H	drag coefficient for momentum, latent heat, and sensible heat, respectively
Ri	bulk Richardson number
τ^λ	longitudinal component of wind stress
τ^φ	latitudinal component of wind stress

Table 2

Values of parameters and constants in the ocean model

Parameter of constant	Symbol	Value	Unit
reference temperature	To	278.2	°C
reference salinity	So	34.72	°/oo
reference density	ρ_o	1.0276	gm/cm^3
thermal expansion coefficient	α	2.75×10^{-4}	$K^{\circ -1}$
saline contraction coefficient	γ	7.5×10^{-4}	$(parts/million)^{-1}$
longitudinal separation	$\Delta\lambda$	2.5	degree
latitudinal separation	$\Delta\varphi$	2.5	degree
longitude at the western boundary	λo	varies	°W
longitude at the eastern boundary	λ_i	varies	°E
latitude of the northern boundary	φ_j	varies	°N
total depth	D	4	km
horizontal eddy viscosity	ν_1	2.5×10^8	cm^2/sec
horizontal eddy diffusivity	κ_1	10^7	cm^2/sec

Table 2 (continued)

Parameter or constant	Symbol	Value	Unit
vertical eddy viscosity	ν_2	1.5	cm^2/sec
vertical eddy diffusivity	κ_2	1	cm^2/sec
earth rotation rate	Ω	7.27×10^{-5}	sec^{-1}
specific heat of sea water	C_p	0.958	cal/gm K
time step	Δt	4.2	hours
Ekman number	E	1.63×10^{-6}	nondimensional
Rossby number	Ro	2.03×10^{-5}	nondimensional
Reynolds number	Re	10	nondimensional
Péclét number	Pé	100	nondimensional
lateral width of frictional boundary layer	L_F	1.2×10^{-2}	nondimensional
lateral width of inertia boundary layer	L_I	4.5×10^{-3}	nondimensional
drag coefficient under neutral state	$(C_D)_N$	2.5×10^{-3}	ergs
constants in drag coefficients	b_1	52.9	ergs
constants in drag coefficients	b_2	53.2	ergs

Table 2 (concluded)

Parameter or constant	Symbol	Value	Unit
constant in Richardson number	β_V, β_T	4.7	
constant in Richardson number	Z_{10}	10^3	cm
constant in Richardson number	T_{vo}	290	K

List of figures

Figure 12. Current streamline plots: (a) at 10-m depth; (b) at 250-m depth; (c) at 1500-m depth.

Figure 13. Surface mean current pattern in the North Pacific Ocean (from U.S. Department of Commerce, 1961): (a) summer; (b) winter.

Figure 14. Vertical velocity contours at different levels in the North Pacific Ocean: (a) at 20-m depth; (b) at 300-m depth; (c) at 2200-m depth.

Figure 15. Temperature distribution at different layers: (a) 10 m; (b) 250 m; (c) 3000 m.

Figure 16. Observational surface temperature distribution in the North Pacific Ocean (from Masuzawa, 1972): (a) summer; (b) winter.

Figure 17. Temperature profiles in the east-west vertical cross sections: (a) 5°N latitude; (b) 15°N latitude; (c) 25°N latitude; (d) 35°N latitude.

Figure 18. Temperature profiles in the cross sections from atlas or observational data: (a) 0°-10°N latitude; (b) 10°-20°N latitude; (c) 20°-30°N latitude (all from Moromtsev, 1963); (d) 35°N latitude (from Masuzawa, 1972).

Figure 19. Temperature profiles in the north-south vertical cross sections: (a) 105°W longitude; (b) 135°W longitude; (c) 175°W longitude; (d) 155°E longitude.

Figure 20. Temperature profiles in the north-south cross sections from atlas and observational data: (a) 100°-110°W longitude; (b) 130°-140°W longitude; (c) 170°-180°W longitude (all from Moromtsev, 1963); (d) 155°E longitude (from Masuzawa, 1972).

Figure 21. Salinity distributions of layers at depths of: (a) 10 m; (b) 250 m; (c) 3000 m.

Figure 22. Average sea surface salinity in North Pacific Ocean (from Reid, 1969): (a) summer; (b) winter.

Figure 23. Salinity profiles in north-south vertical cross sections at: (a) 105°W longitude; (b) 165°E longitude; (c) 180°W longitude.

Figure 24. Observational salinity profiles in the north-south vertical cross sections: (a) 100°-110°W longitude; (b) 160°-170°W longitude (all from Moromtsev, 1963); (c) 180°W longitude (from Moromtsev, 1963).

Figure 25. Pressure distributions: (a) at surface; (b) at 300-m depth; (c) at 2250-m depth. Contour interval is 0.6 m^2/sec^2.

Figure 26. Annual mean dynamic height in dynamic meters with respect to 1000-m reference level (from Wyrtki, 1974).

Figure 27. Energetic diagrams in the NORPAX model. Units for energy are $ergs/cm^3$, and for rate of energy transformation, $ergs/cm^3/day$.

Figure 28. Zonally averaged meridional heat transport in the model. H_T indicates total northward heat transport; H_v, heat transport due to total current; $H_{v'}$, heat transport due to baroclinic current; $H_{\bar{v}}$, heat transport due to barotropic current; H_d, heat transport due to diffusion processes.

Figure 29. Total meridional heat transport in the North Pacific Ocean: (a) from the ocean model (NPO); (b) from Vonder-Haar and Oort (1973), (VO); (c) from Budyko (1963) and Sellers (1965), (BS).

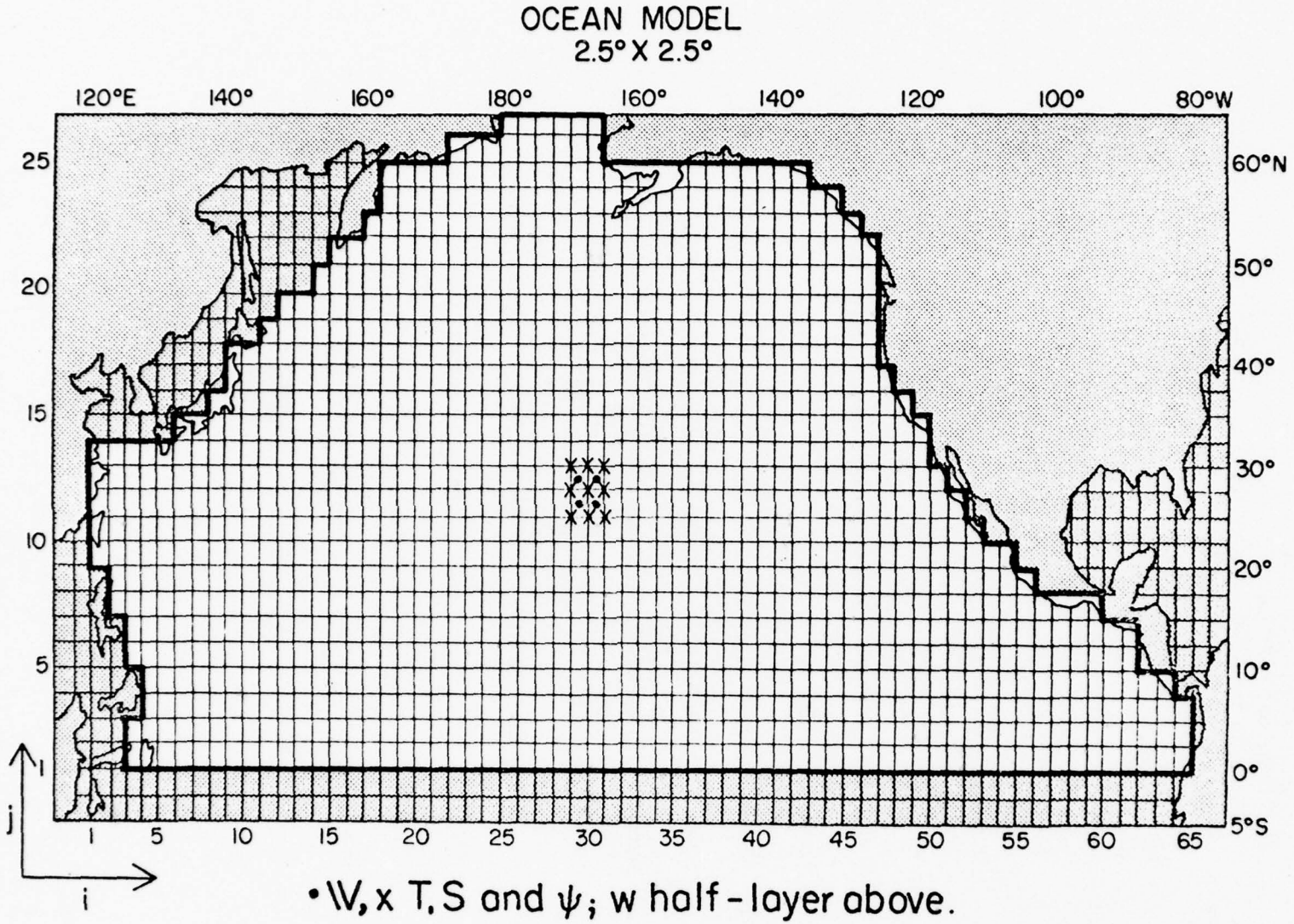
OCEAN MODEL
2.5° X 2.5°
120°E
140°
160°
180°
160°
140°
120°
100°
80°W
60°N
50°
40°
30°
20°
10°
0°
5°S
25
20
15
10
5
1
1
5
10
15
20
25
30
35
40
45
50
55
60
65
j
i
• V, x T, S and ψ; w half-layer above.

Figure 1

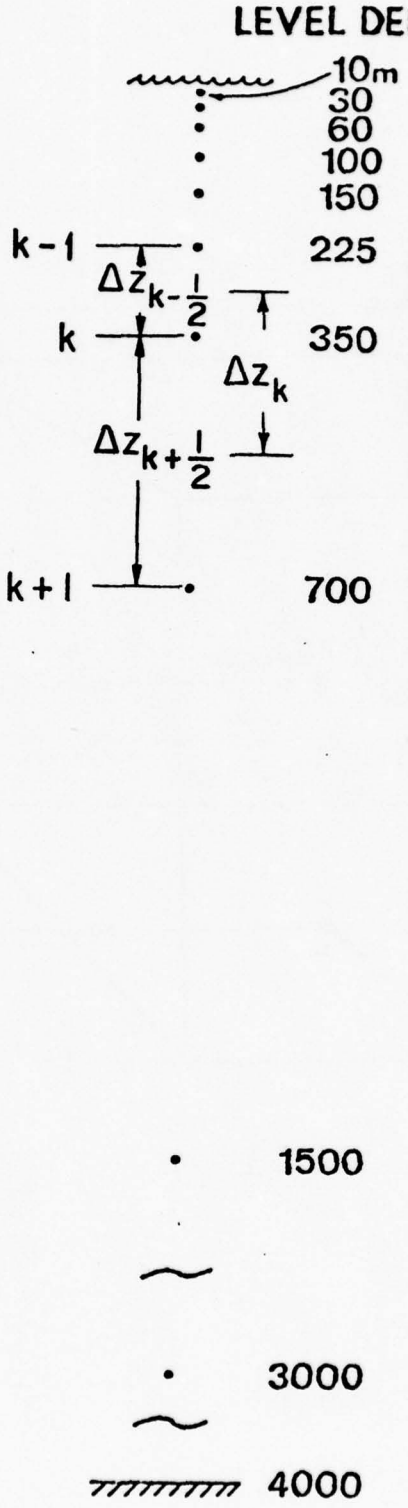
LEVEL DEPTHS
10m
30
60
100
150
k-1
225
$\Delta z_{k-\frac{1}{2}}$
k
350
Δz_k
$\Delta z_{k+\frac{1}{2}}$
k+1
700
1500
3000
4000

Figure 2

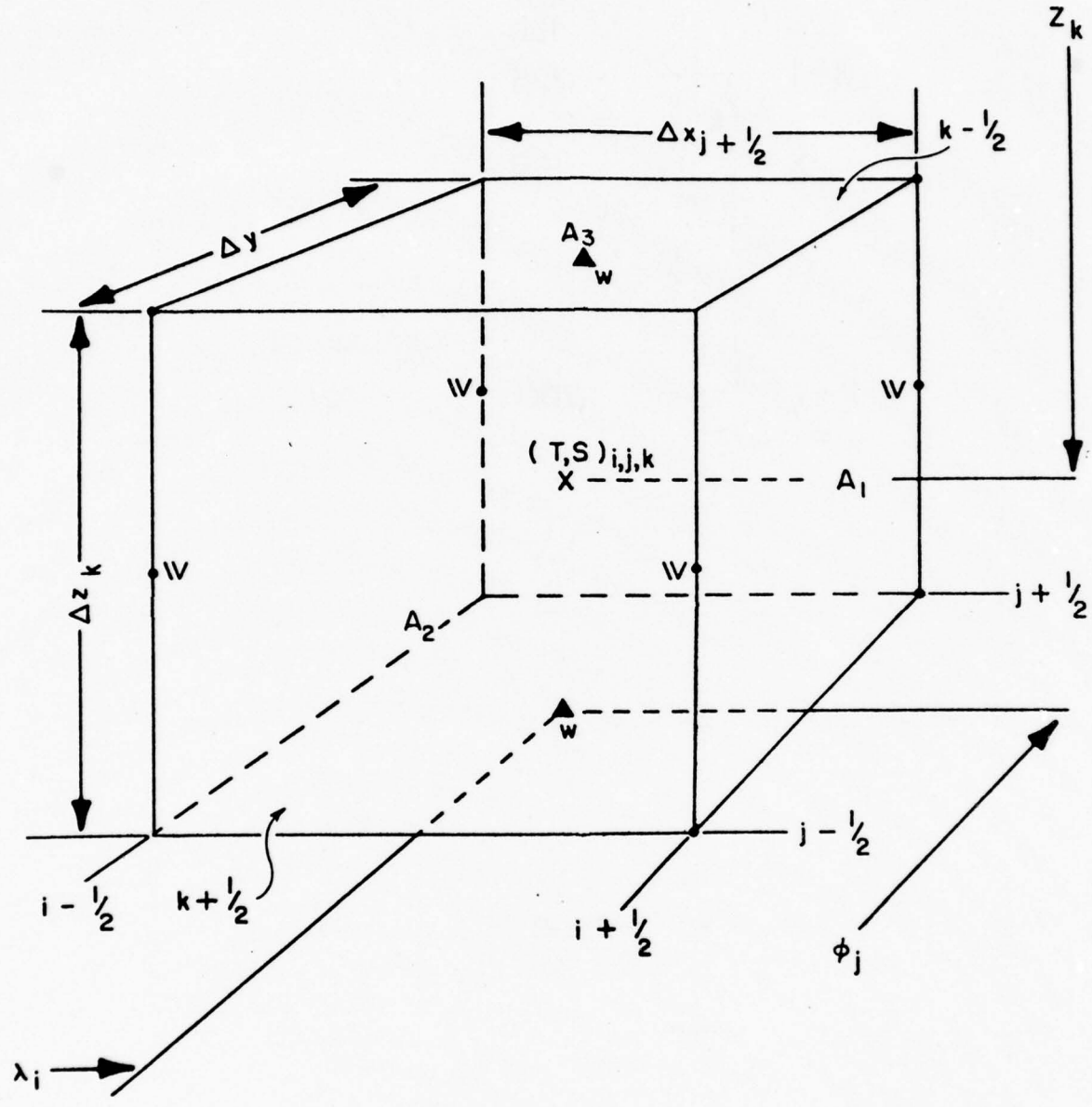
Z_k
$\Delta x_{j+1/2}$
$k-1/2$
Δy
A_3
w
Δz_k
$(T,S)_{i,j,k}$
A_1
A_2
$j+1/2$
$j-1/2$
$i-1/2$
$k+1/2$
$i+1/2$
ϕ_j
λ_i

Figure 3

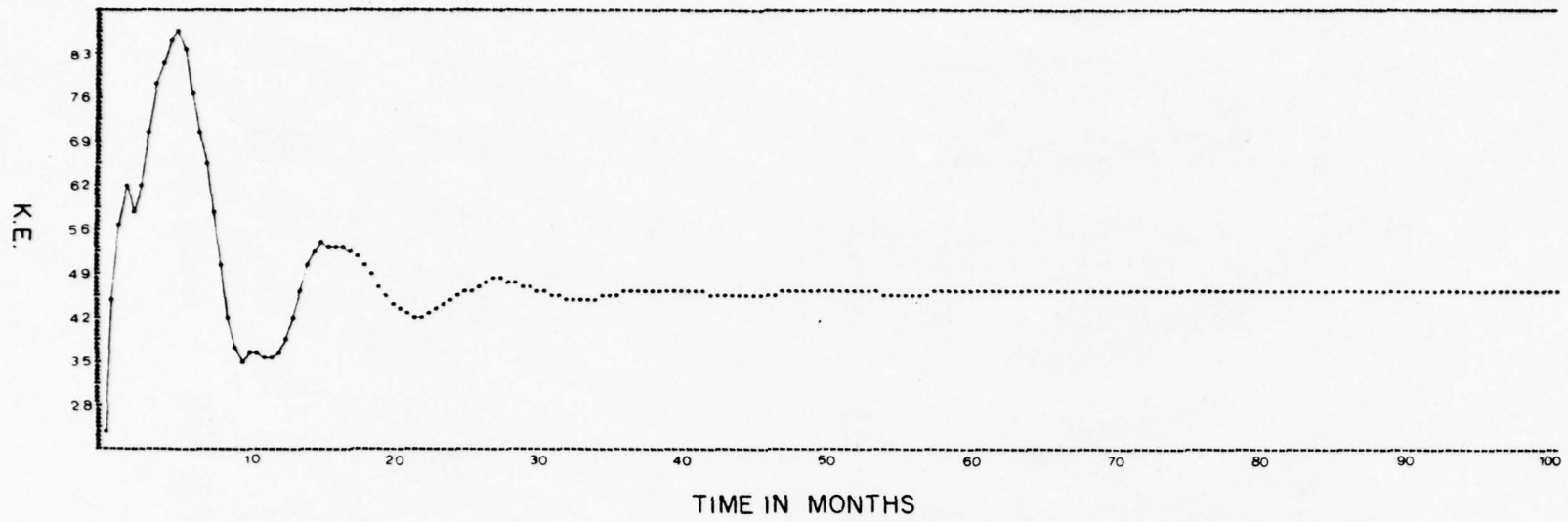
K.E.
83
76
69
62
56
49
42
35
28
10
20
30
40
50
60
70
80
90
100
TIME IN MONTHS

Figure 4

RELATIVE WEIGHT OF TERMS IN MOMENTUM EQUATION (%)

(REGION: KUROSHIO 35°N, 140°E)

X MOMENTUM EQUATION

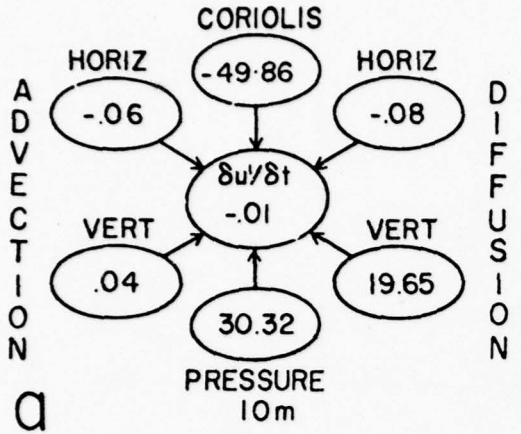

a

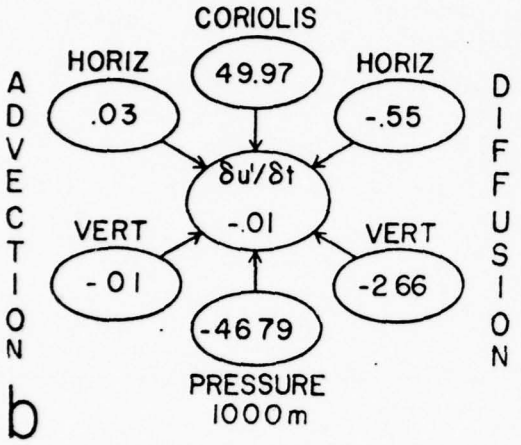

b

Y MOMENTUM EQUATION

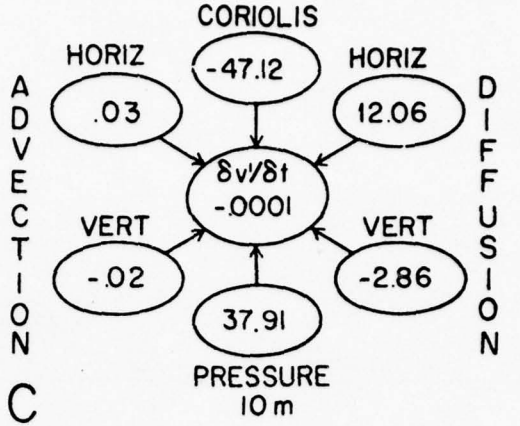

C

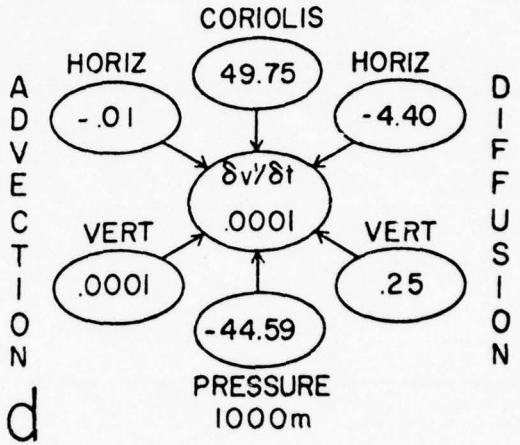

d

Figure 5

RELATIVE WEIGHT OF TERMS IN MOMENTUM EQUATION (%)

(REGION: EQUATOR 25°N, 165°W)

X MOMENTUM EQUATION

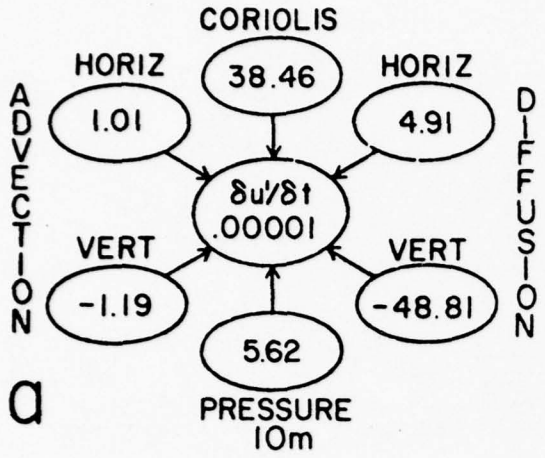

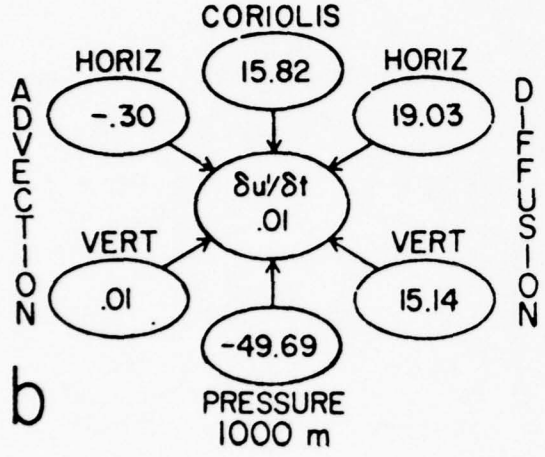

Y MOMENTUM EQUATION

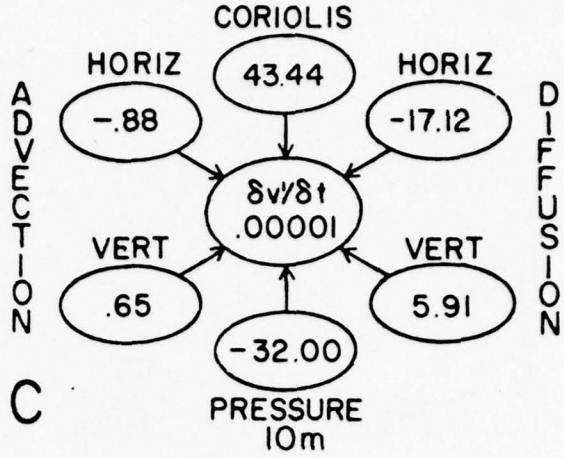

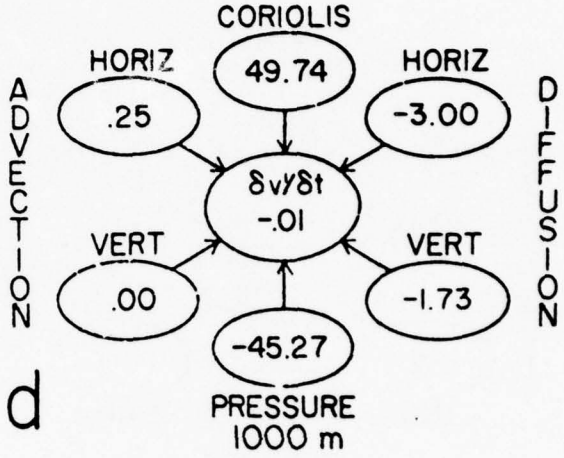

Figure 6

RELATIVE WEIGHT OF TERMS IN MOMENTUM EQUATION (%)

(REGION: MID-OCEAN 30°N, 160°W)

X MOMENTUM EQUATION

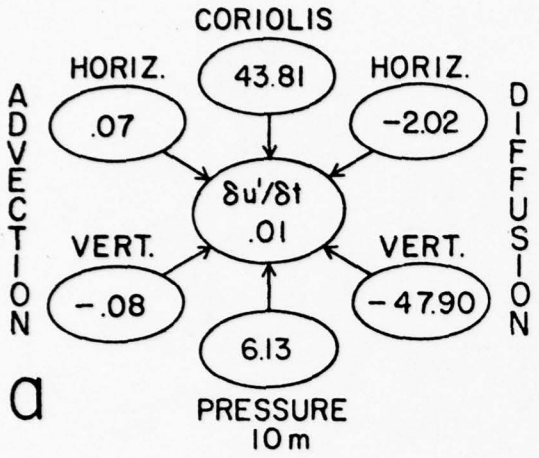

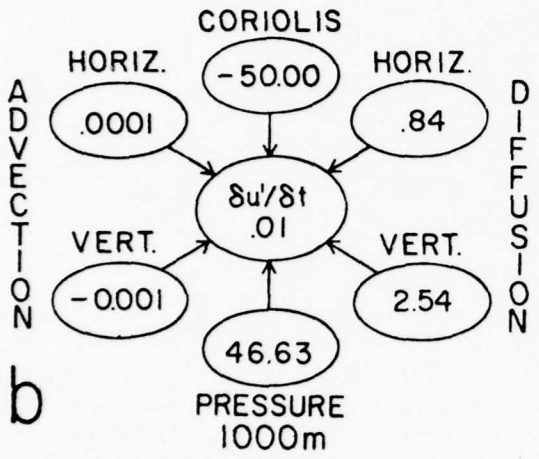

Y MOMENTUM EQUATION

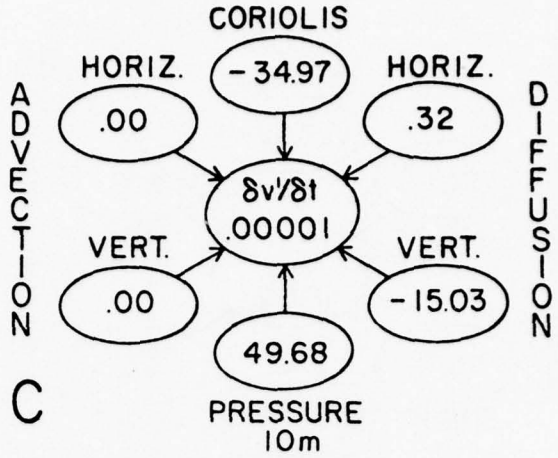

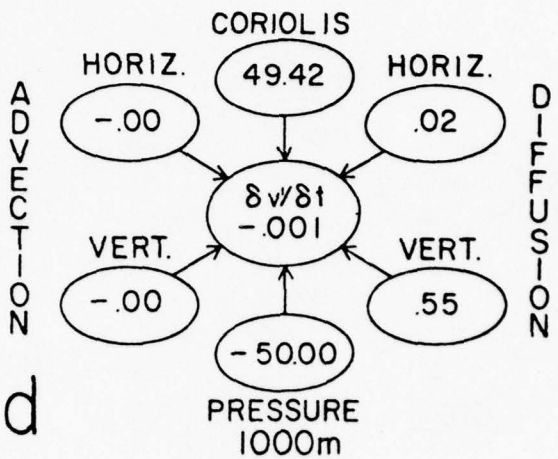

Figure 7

RELATIVE WEIGHT OF TERMS (%) (Equatorial Region. 0°N, 165°W)

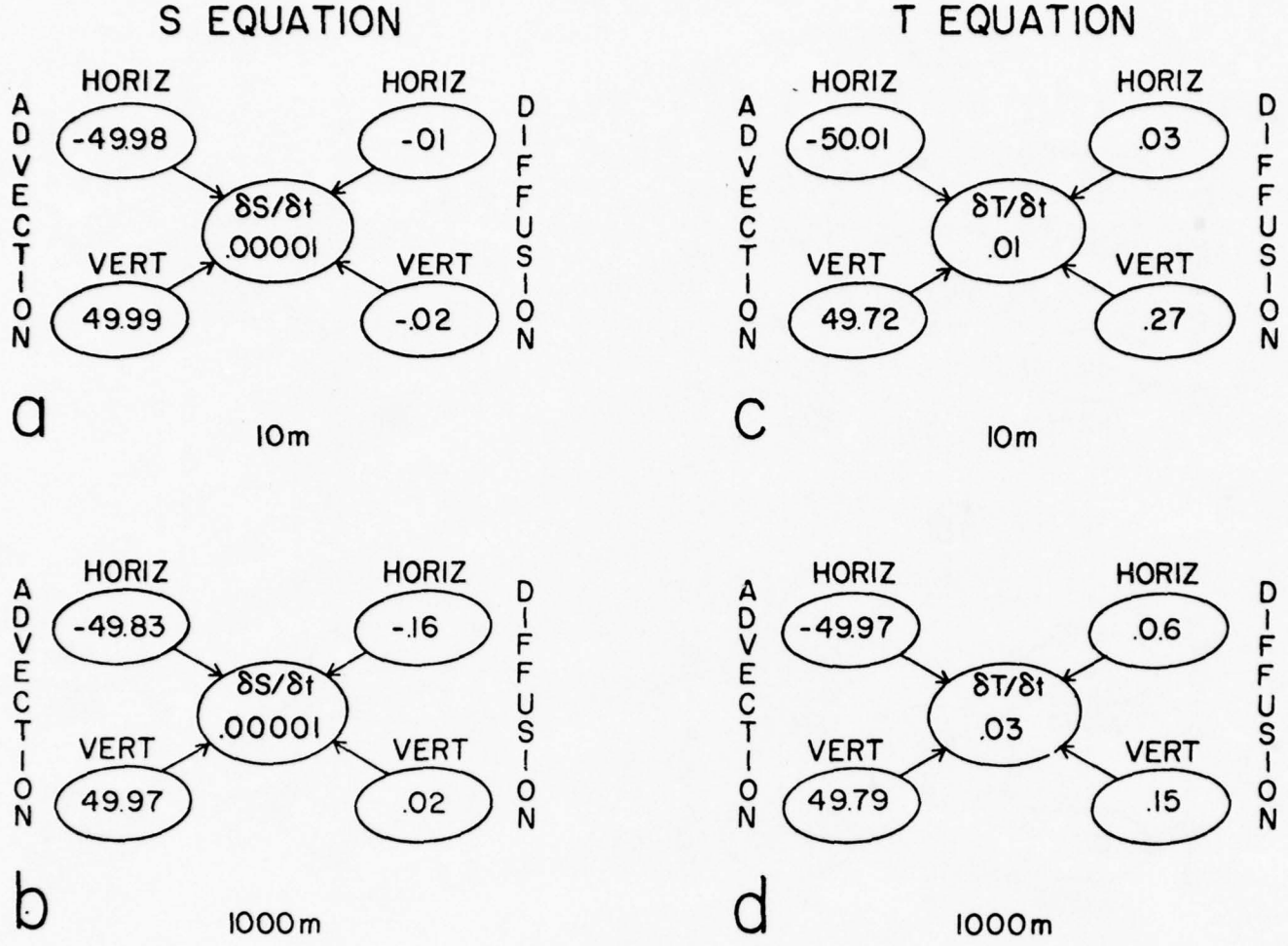

Figure 8

RELATIVE WEIGHT OF TERMS (%) (Mid-Ocean Region. 35°N, 165°W)

S EQUATION

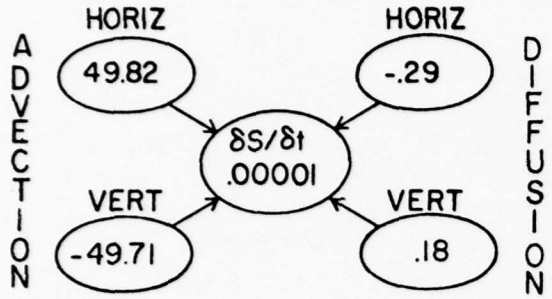

a

10m

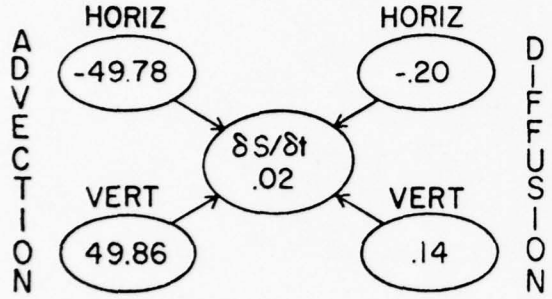

b

1000 m

T EQUATION

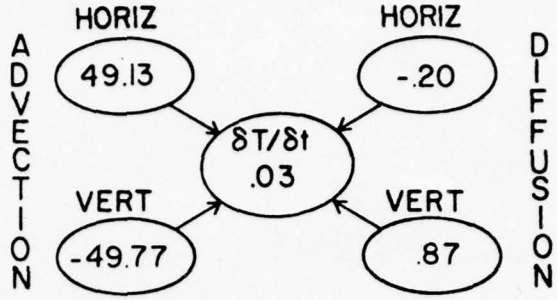

c

10m

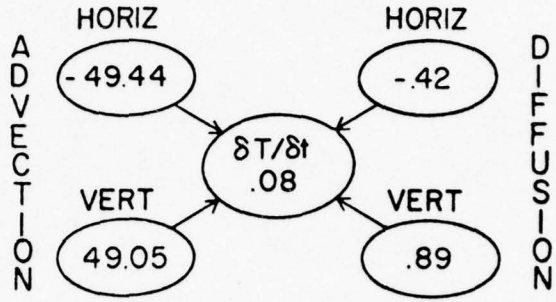

d

1000 m

Figure 9

STREAMFUNCTION

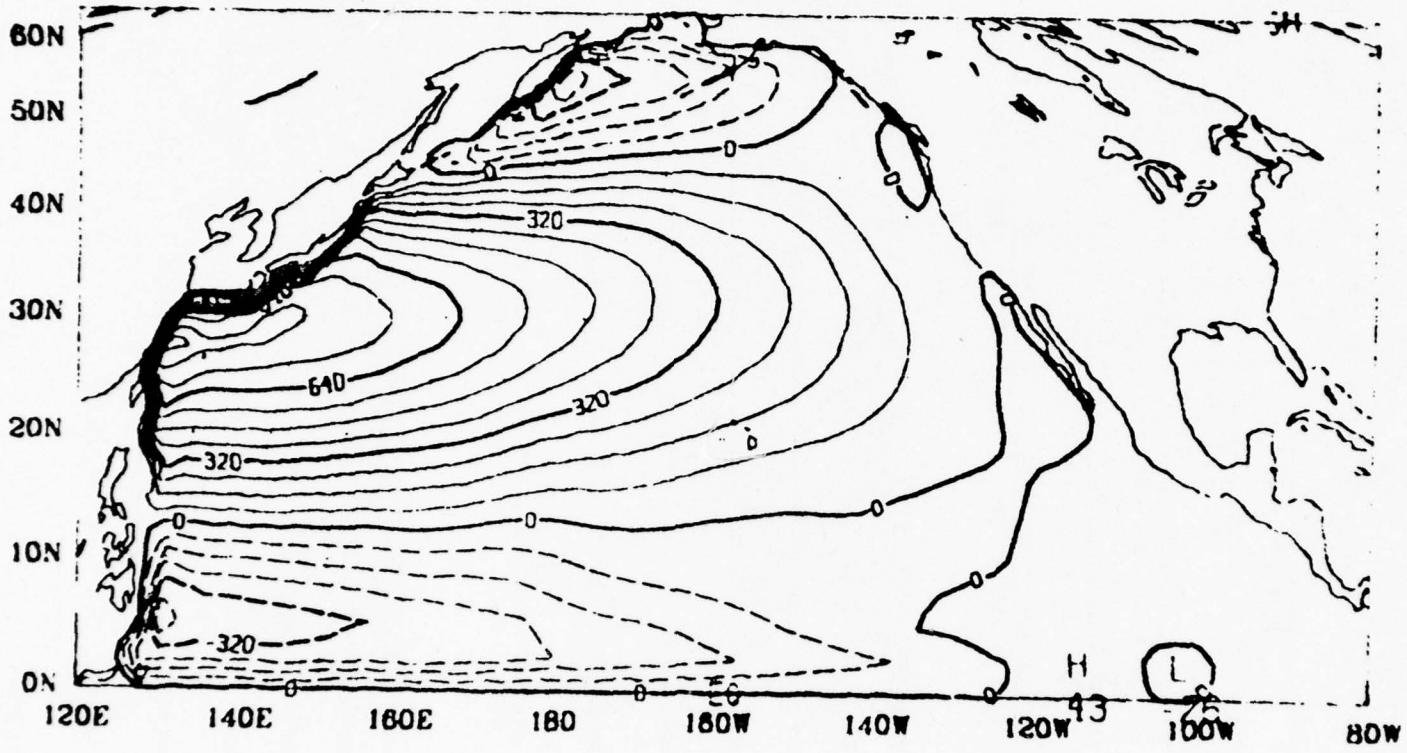

Figure 10

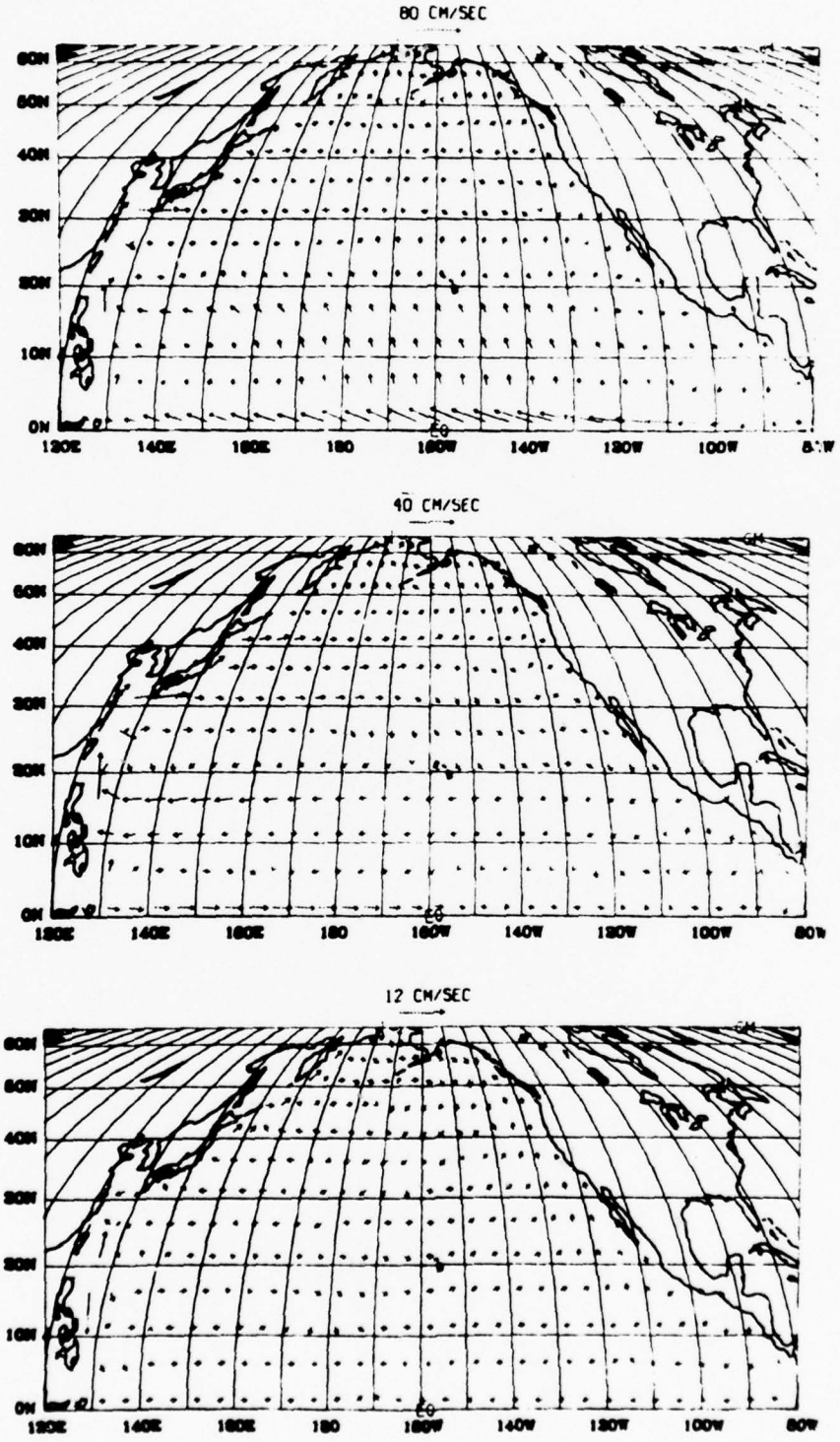
80 CM/SEC
60N
50N
40N
30N
20N
10N
0N
120E
140E
160E
180
160W
140W
120W
100W
40 CM/SEC
12 CM/SEC

Figure 11

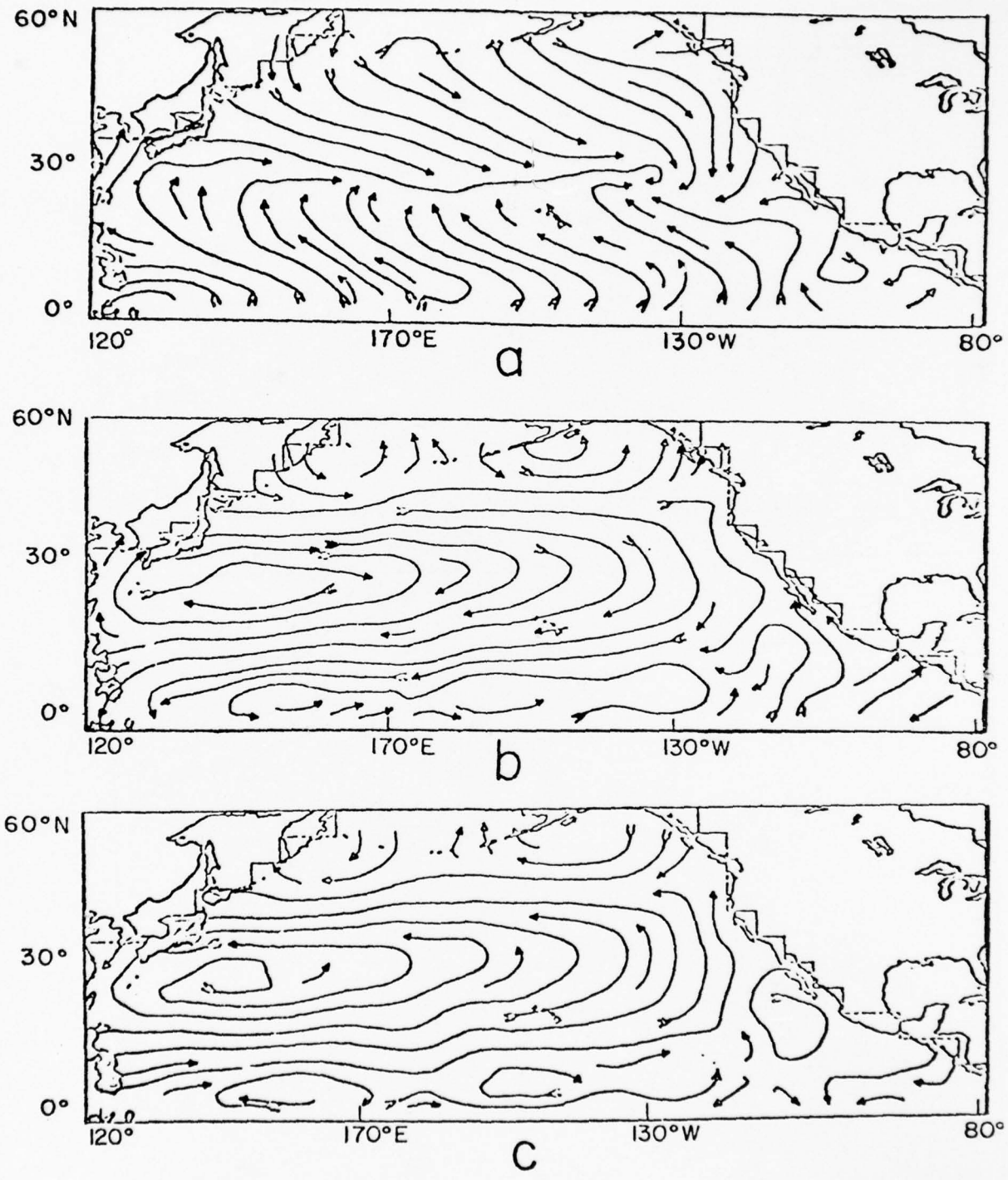
60°N
30°
0°
120°
170°E
130°W
80°
a
60°N
30°
0°
120°
170°E
130°W
80°
b
60°N
30°
0°
120°
170°E
130°W
80°
c

Figure 12

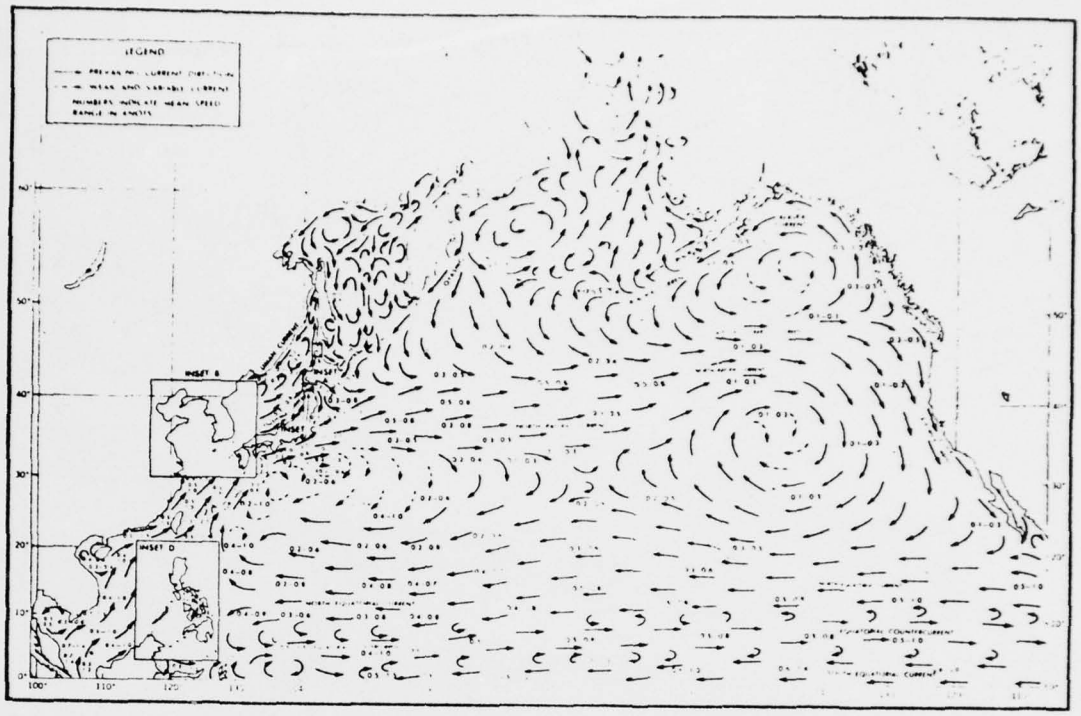
LEGEND
INSET B
INSET D

a

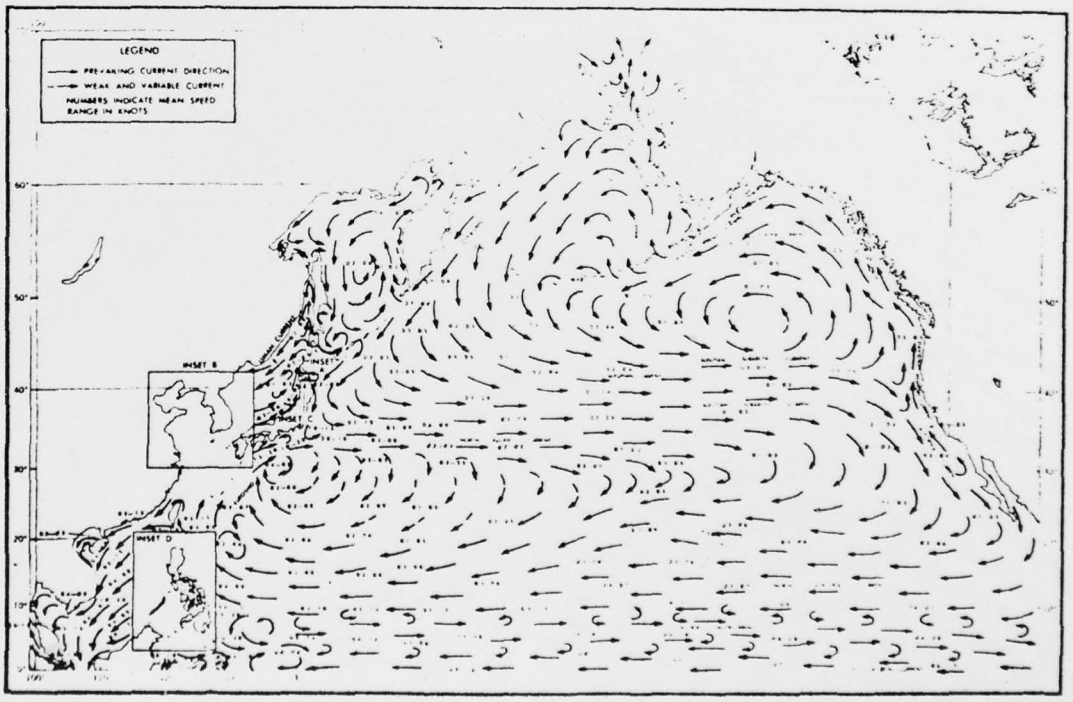
LEGEND
PREVAILING CURRENT DIRECTION
WEAK AND VARIABLE CURRENT
NUMBERS INDICATE MEAN SPEED RANGE IN KNOTS
INSET B
INSET D

b

Figure 13

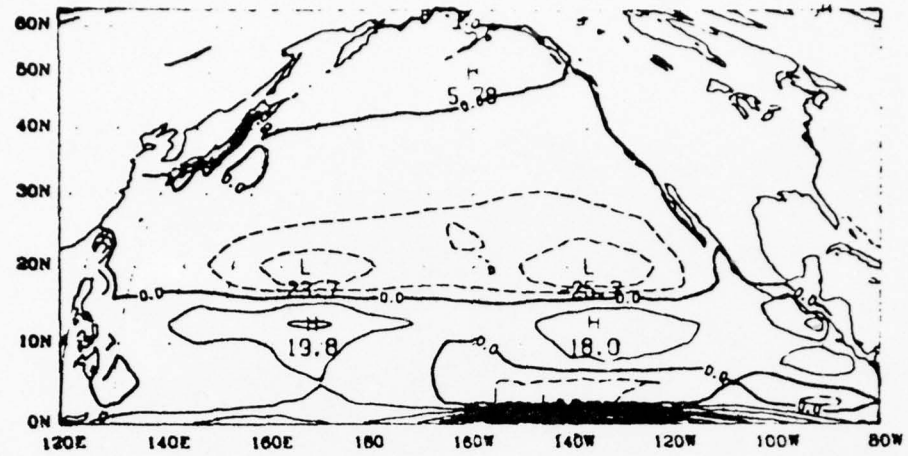
60N
50N
40N
30N
20N
10N
0N
120E
140E
160E
180
160W
140W
120W
100W
80W
5.28
L
23.7
L
25.3
19.8
18.0
0.0

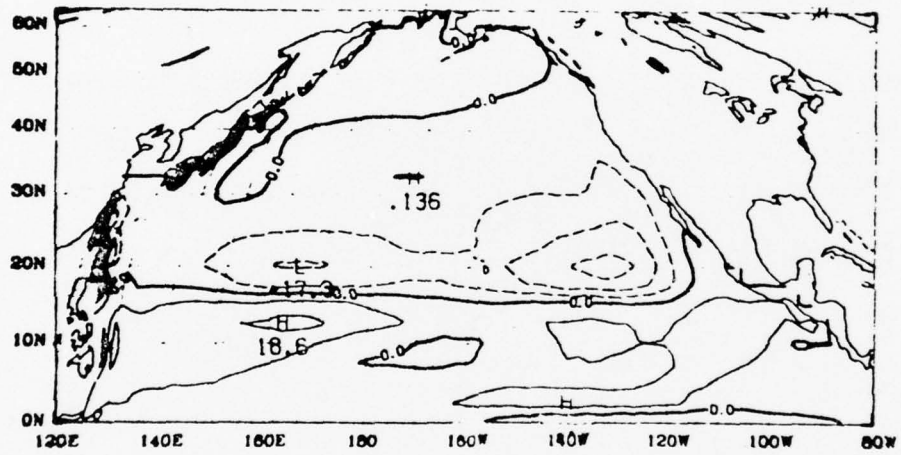
60N
50N
40N
30N
20N
10N
0N
120E
140E
160E
180
160W
140W
120W
100W
80W
.136
18.6
0.0

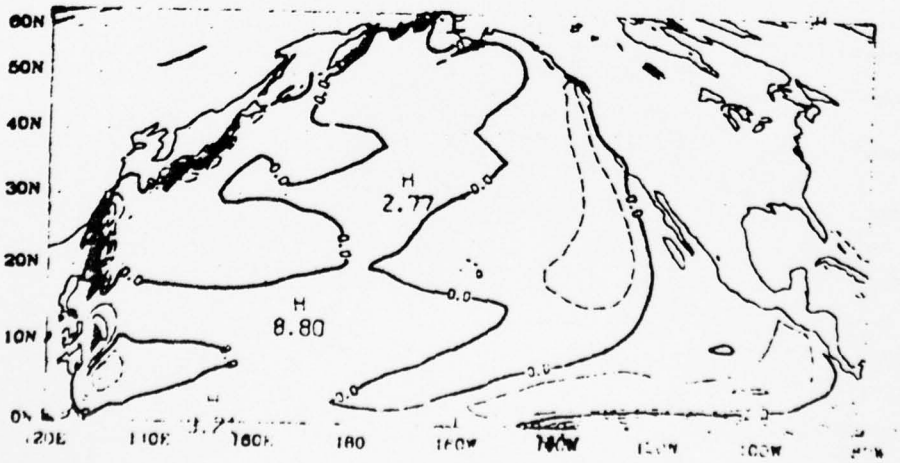
60N
50N
40N
30N
20N
10N
2.77
8.80
0.0

Figure 14

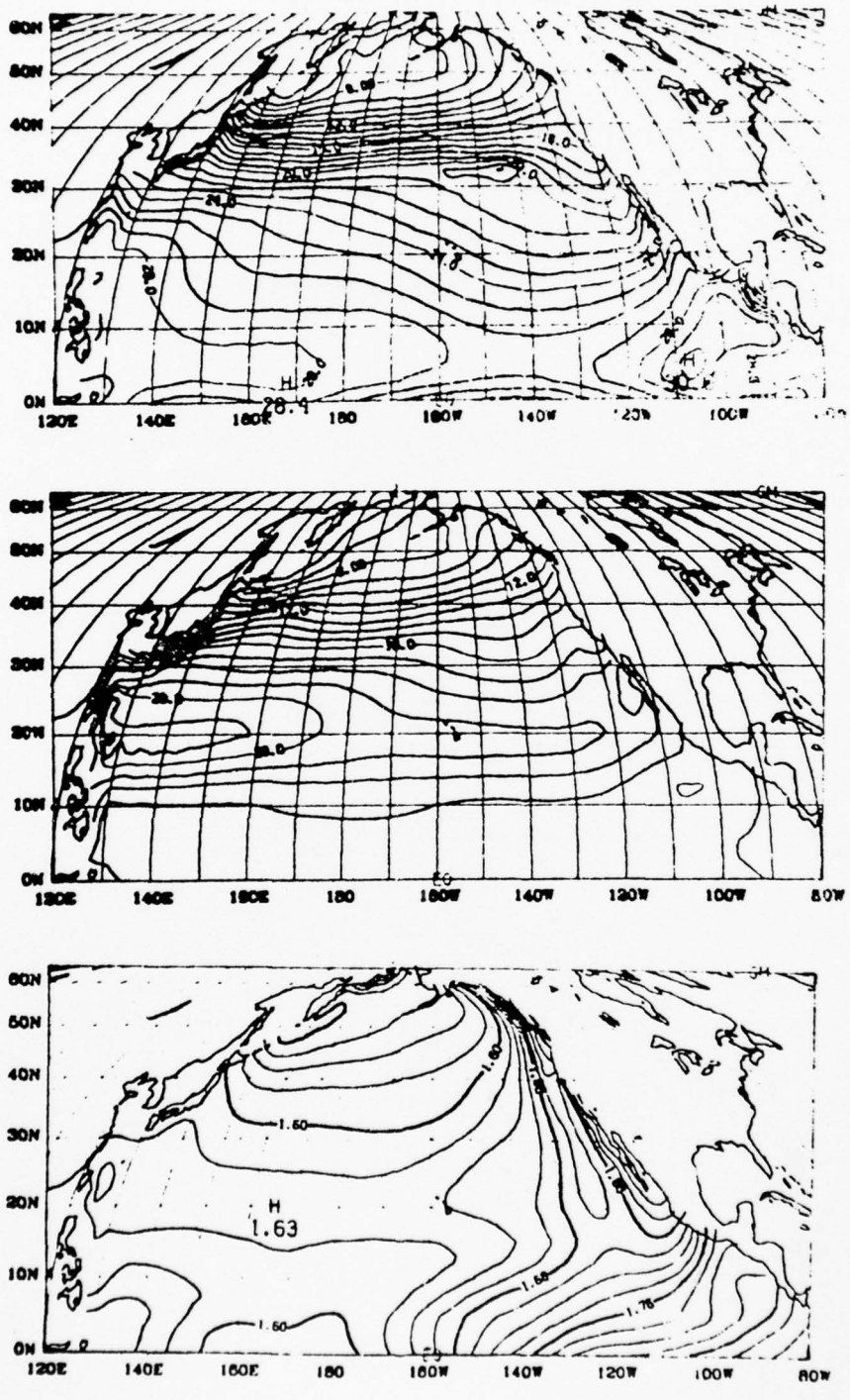
60N
50N
40N
30N
20N
10N
0N
120E
140E
160E
180
160W
140W
120W
100W
80W
H
28.9
1.63
1.60
1.65
1.70
1.75
Eq

Figure 15

(a)

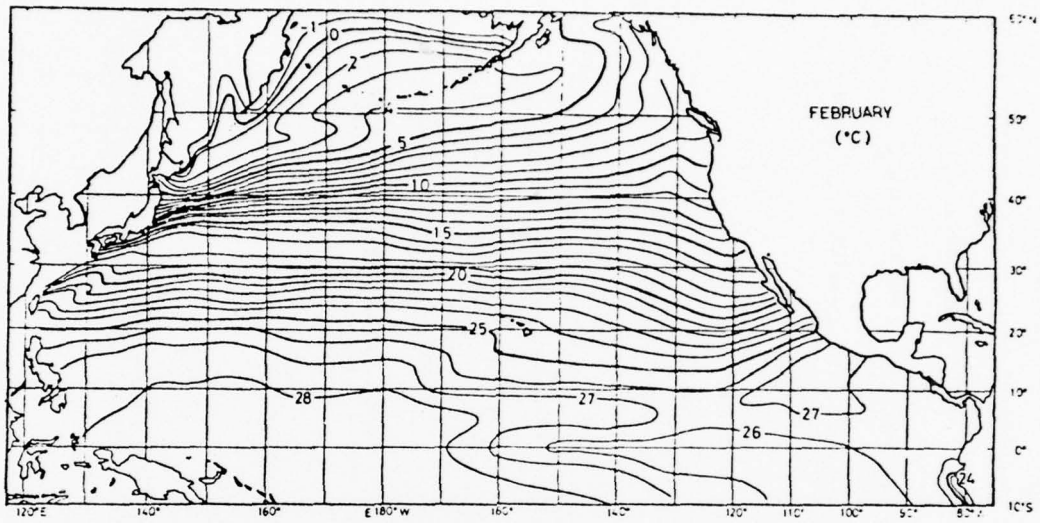
FEBRUARY
(°C)
-1
0
2
5
10
15
20
25
28
27
27
26
24
120°E
140°
160°
E 180° W
160°
140°
120°
110°
100°
50°
80°W
60°N
50°
40°
30°
20°
10°
0°
10°S

(b)

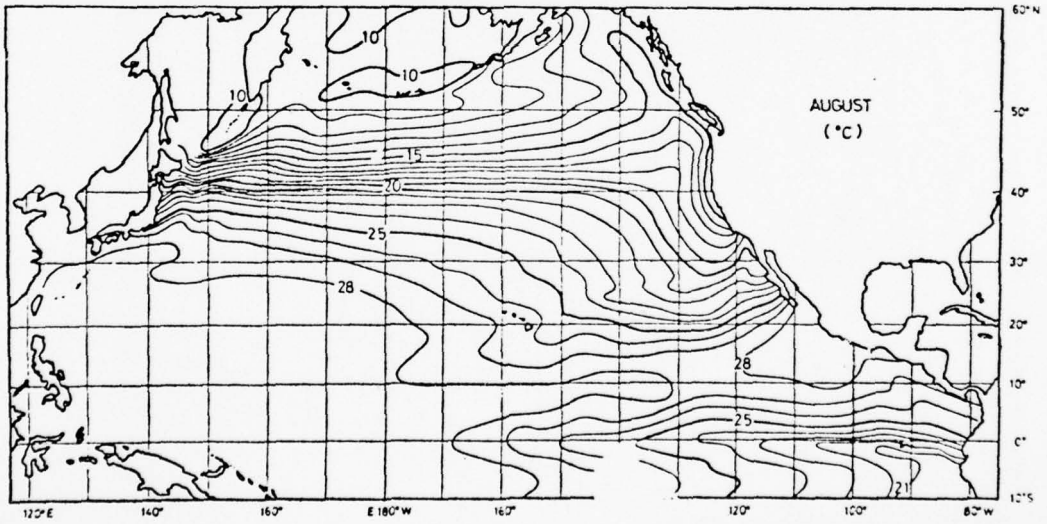
AUGUST
(°C)
10
10
10
15
20
25
28
28
25
21
120°E
140°
160°
E 180° W
160°
120°
100°
80°W
60°N
50°
40°
30°
20°
10°
0°
10°S

Figure 16

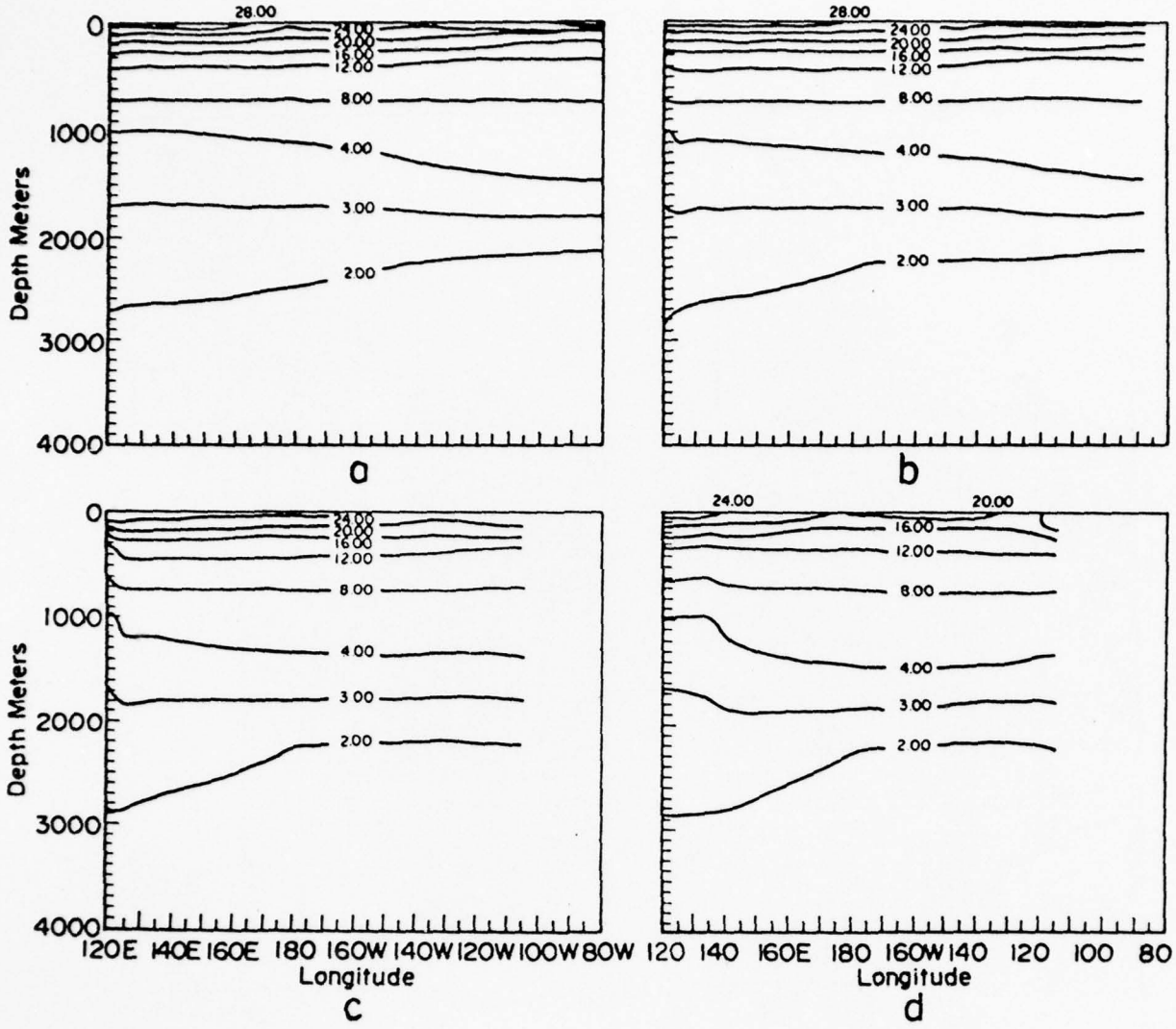
28.00
24.00
20.00
16.00
12.00
8.00
4.00
3.00
2.00
0
1000
2000
3000
4000
Depth Meters
a
b
c
d
120E 140E 160E 180 160W 140W 120W 100W 80W
120 140 160E 180 160W 140 120 100 80
Longitude

Figure 17

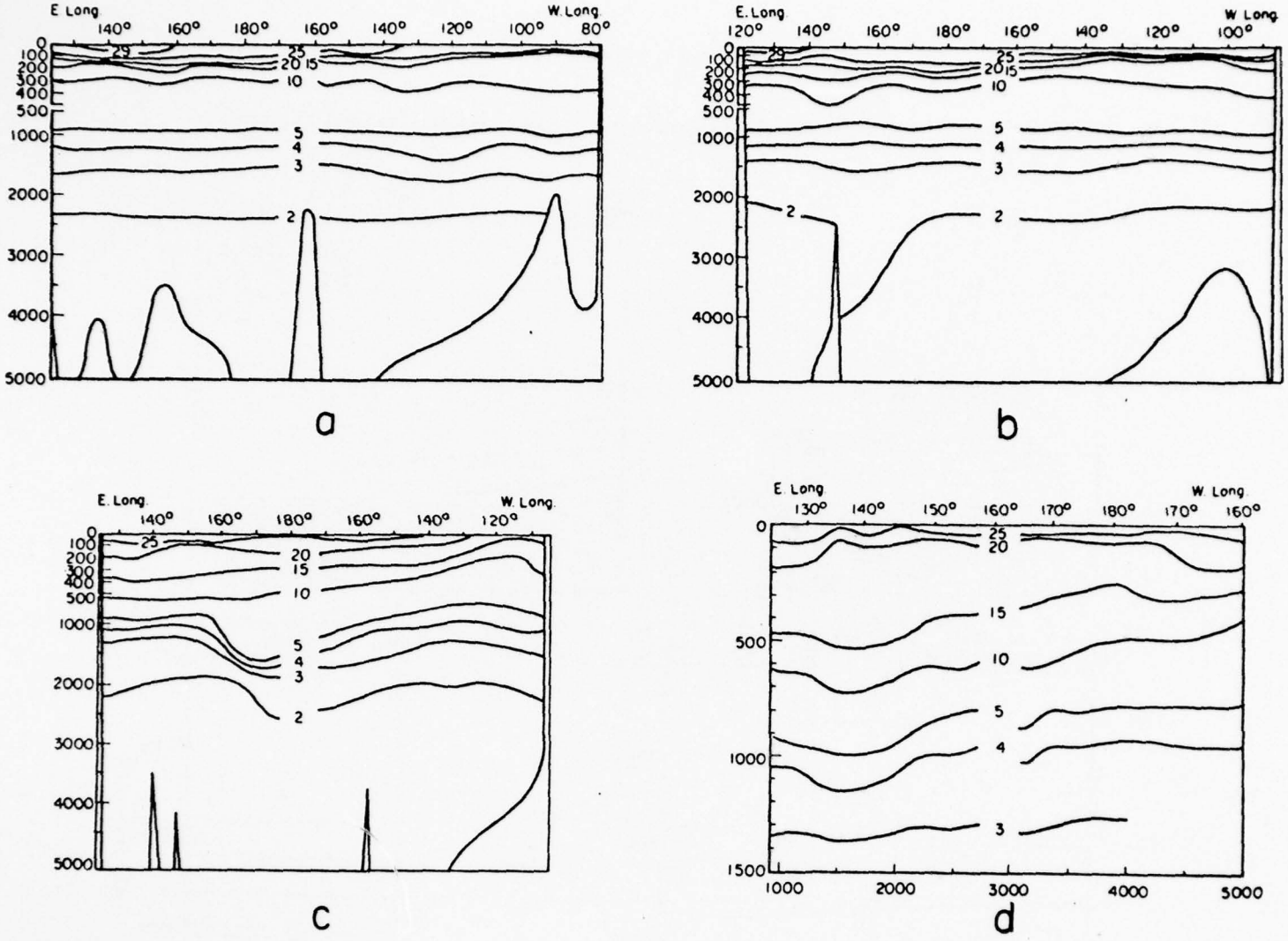
E. Long.
W. Long.
140° 160° 180° 160° 140° 120° 100° 80°
0
100
200
300
400
500
1000
2000
3000
4000
5000
29
25
20
15
10
5
4
3
2
a
E. Long.
W. Long.
120° 140° 160° 180° 160° 140° 120° 100°
b
E. Long.
W. Long.
140° 160° 180° 160° 140° 120°
c
E. Long.
W. Long.
130° 140° 150° 160° 170° 180° 170° 160°
0
500
1000
1500
1000 2000 3000 4000 5000
d

Figure 18

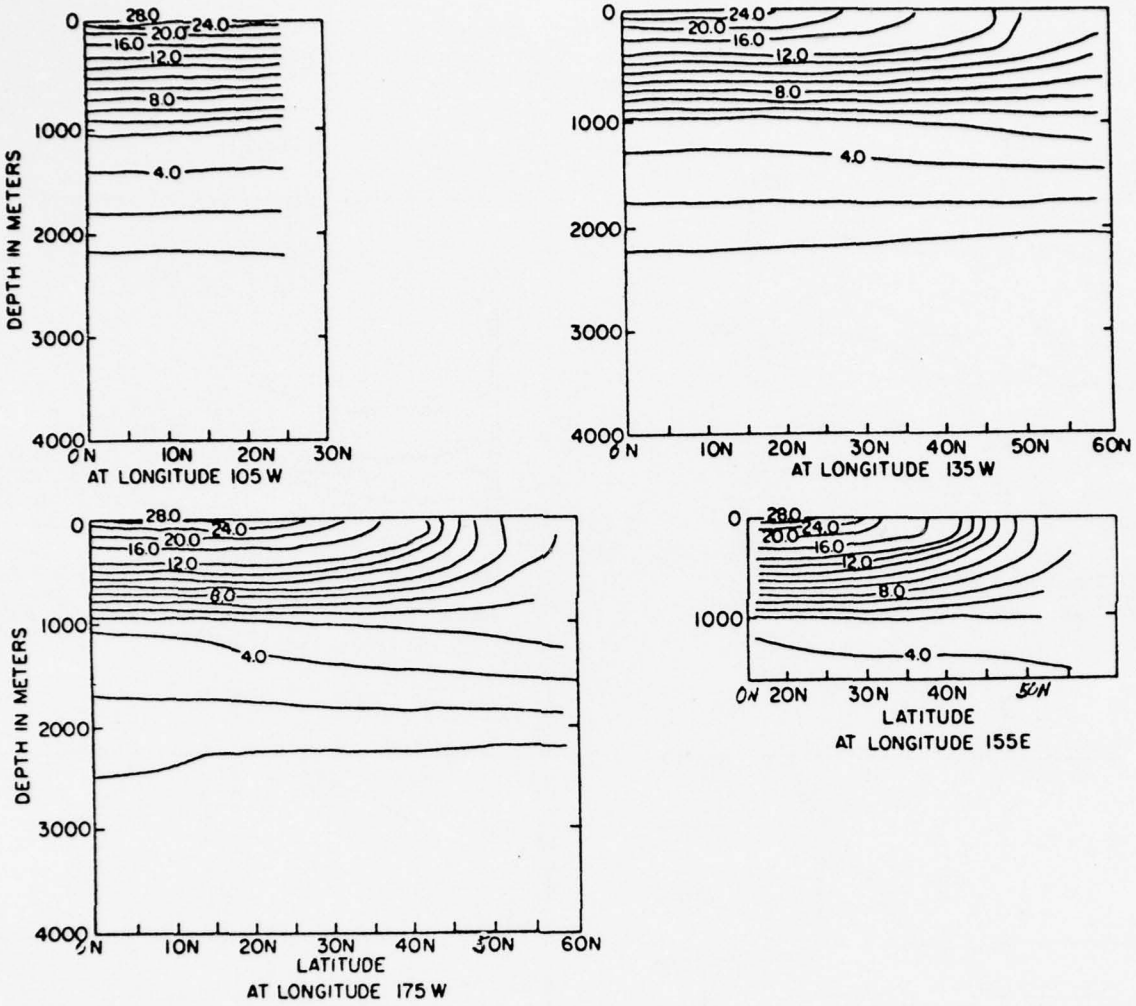

North-South Temperature Profile in the North Pacific Ocean

Figure 19

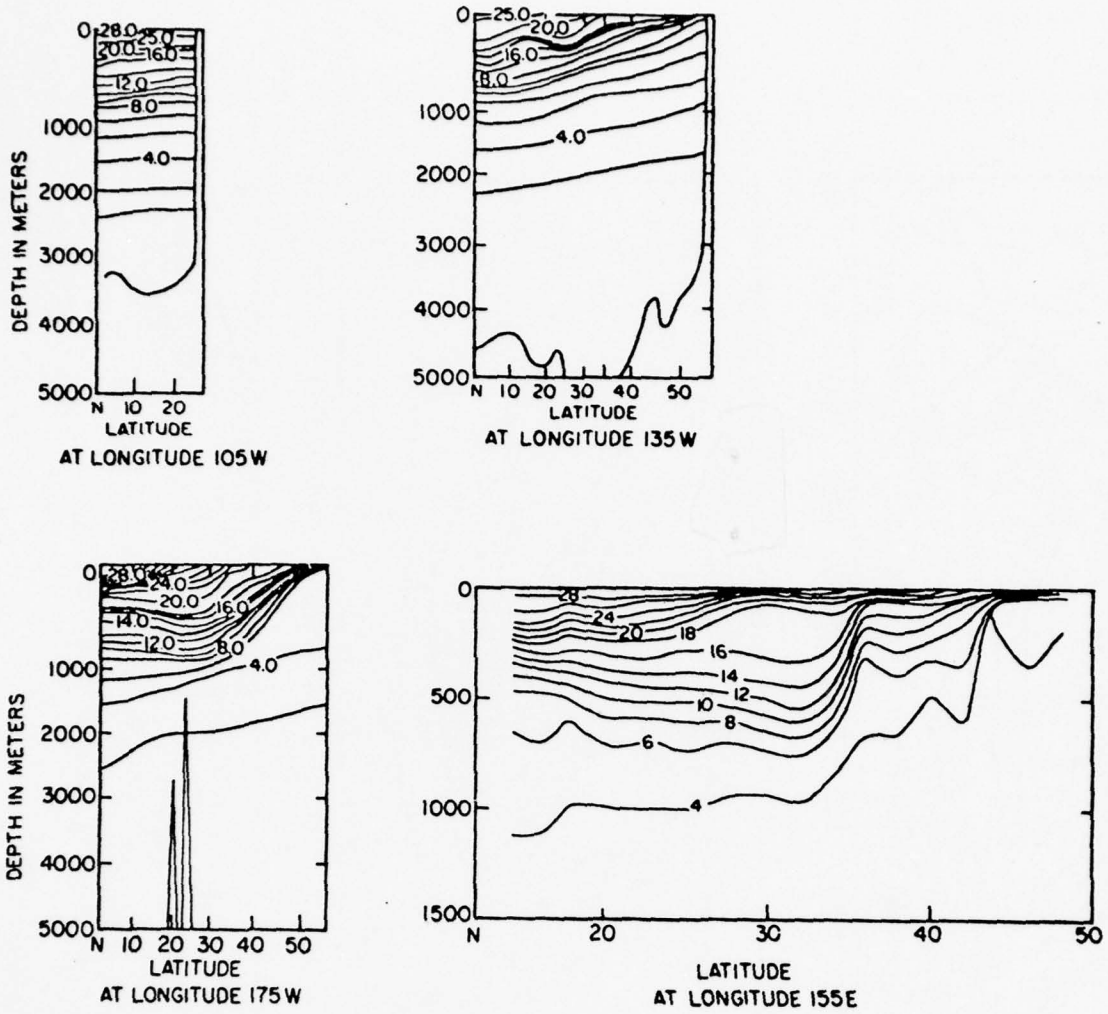

Observed North-South Cross-Section of Temperature Profile in the North Pacific Ocean

Figure 20

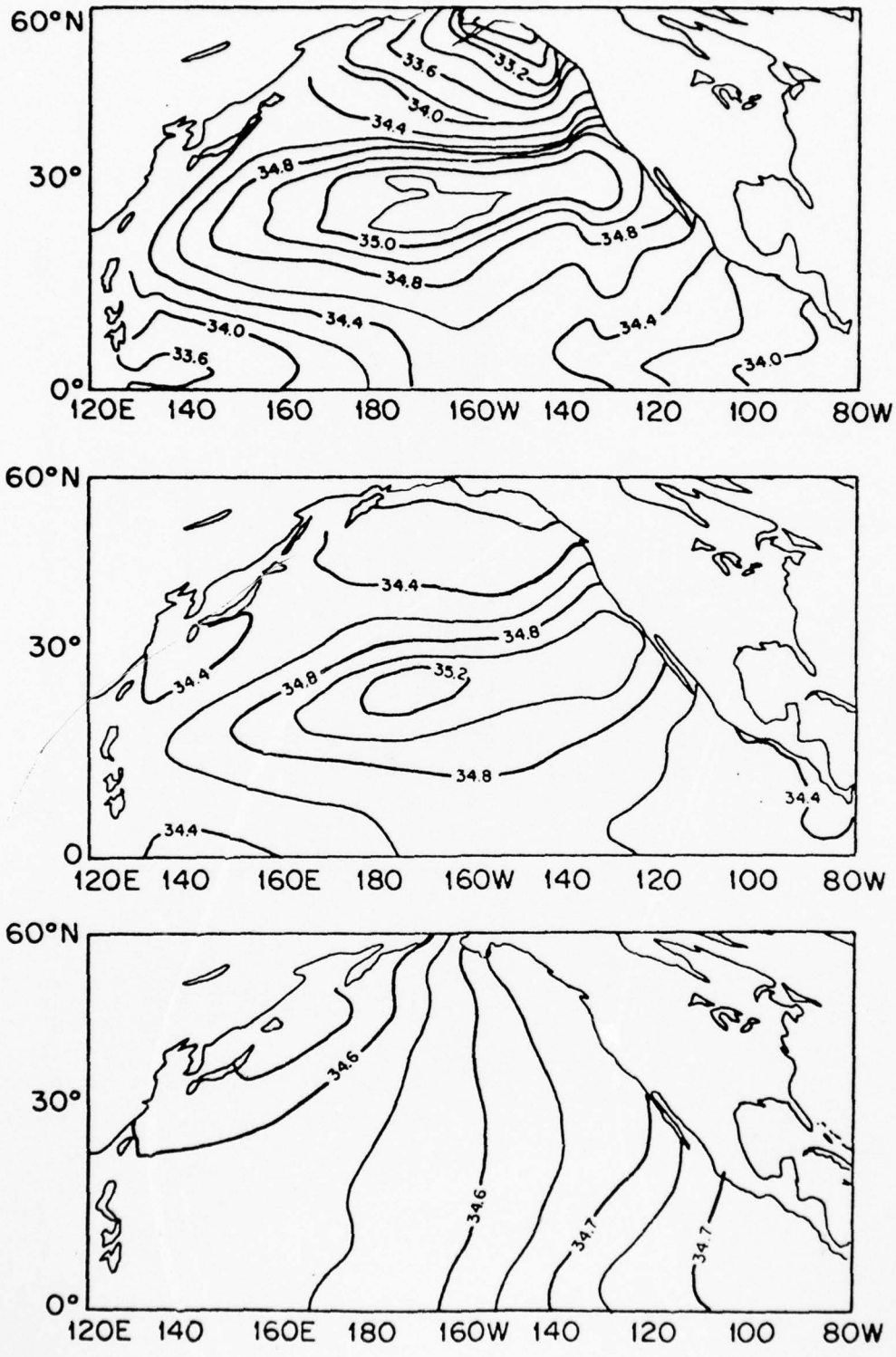
60°N
30°
0°
120E 140 160 180 160W 140 120 100 80W
33.6
33.2
34.0
34.4
34.8
35.0
34.8
34.8
34.4
34.0
33.6
34.4
34.0
60°N
30°
0
120E 140 160E 180 160W 140 120 100 80W
34.4
34.8
34.4
34.8
35.2
34.8
34.4
34.4
60°N
30°
0°
120E 140 160E 180 160W 140 120 100 80W
34.6
34.6
34.7
34.7

Figure 21

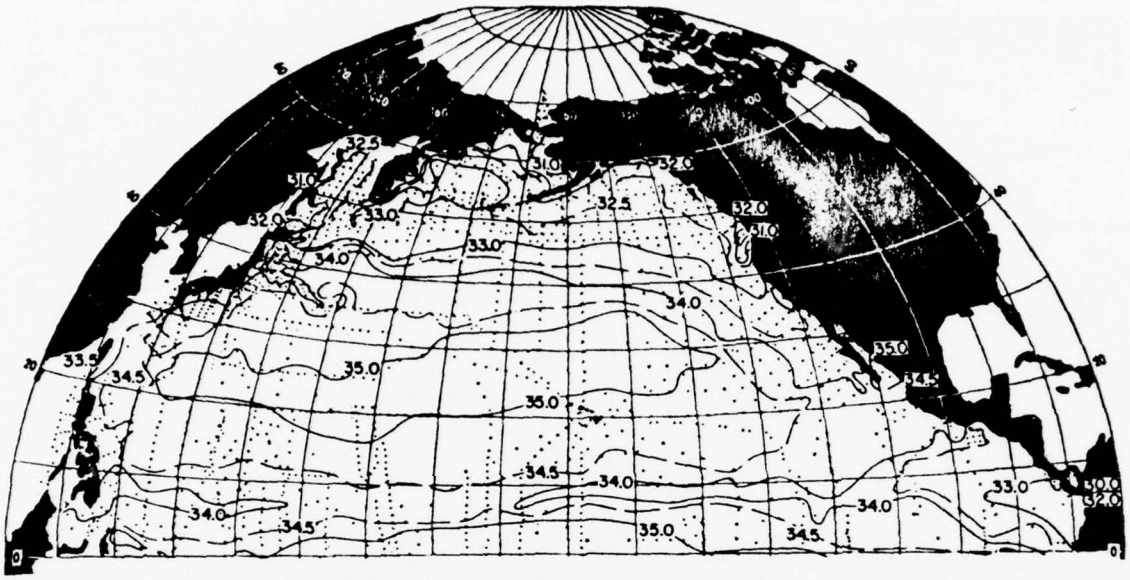

a

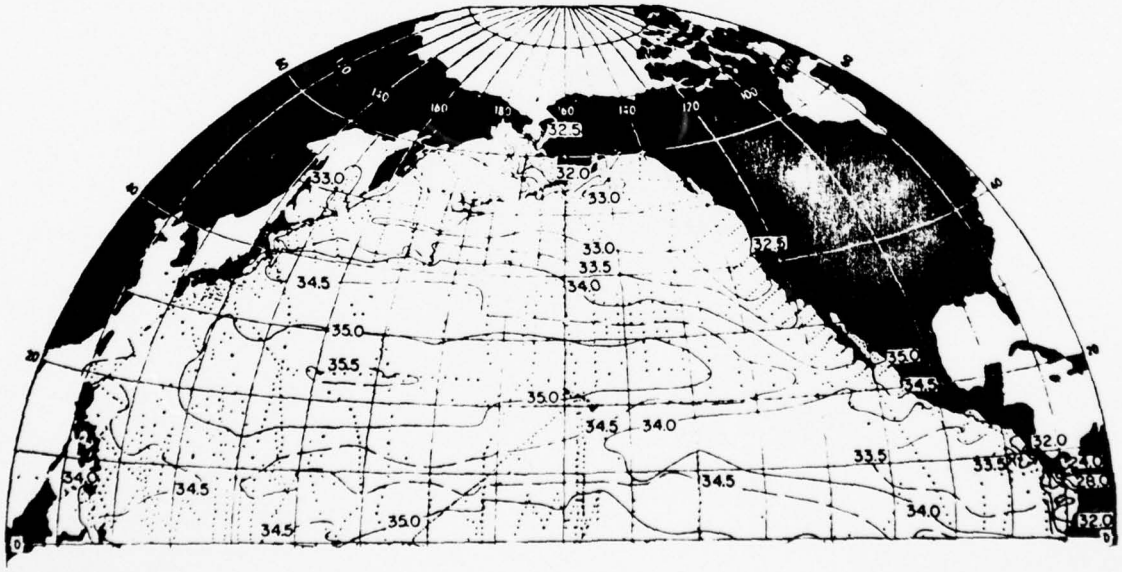

b

Figure 22

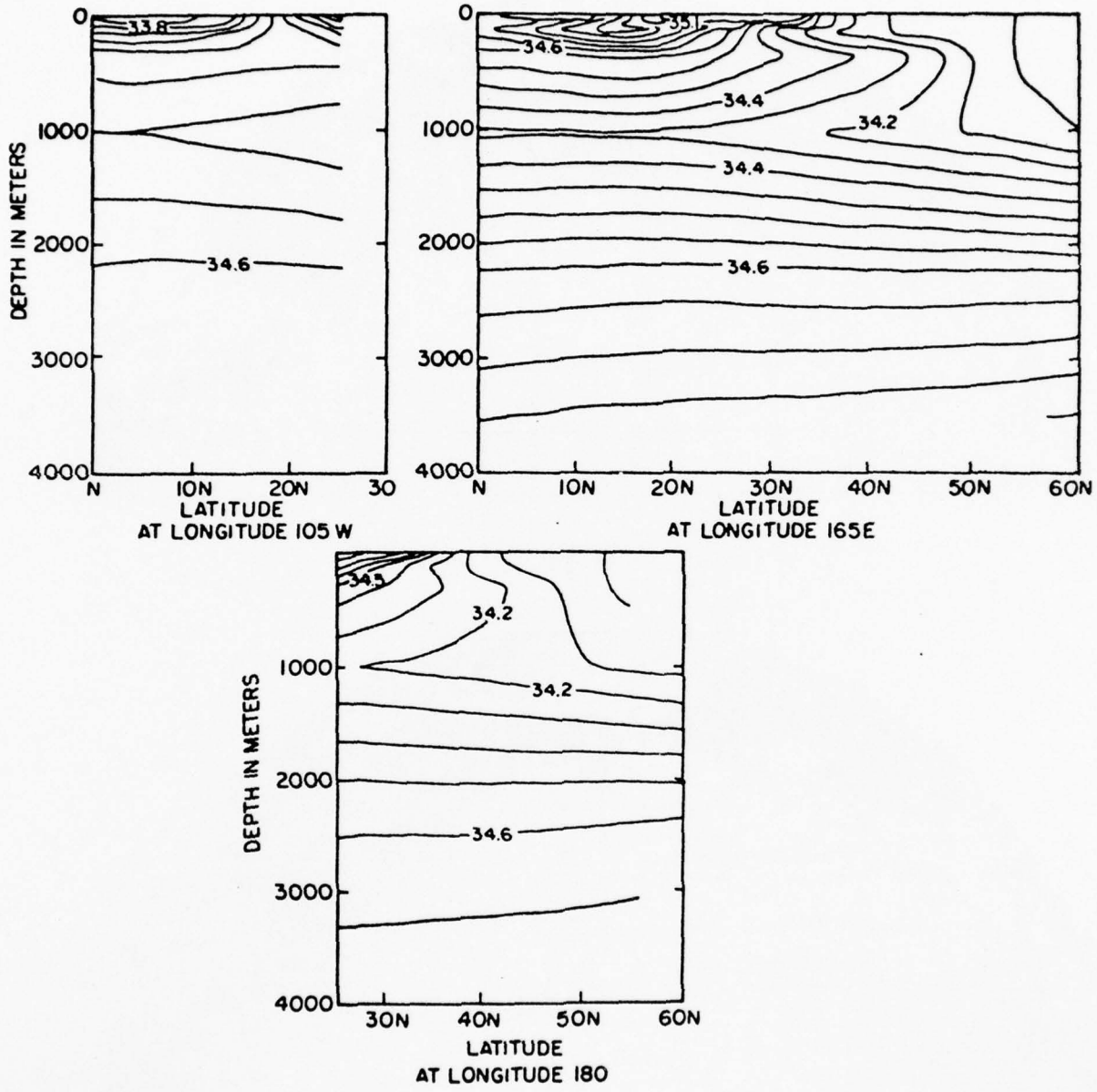

North-South Salinity Profile in the North Pacific Ocean

Figure 23

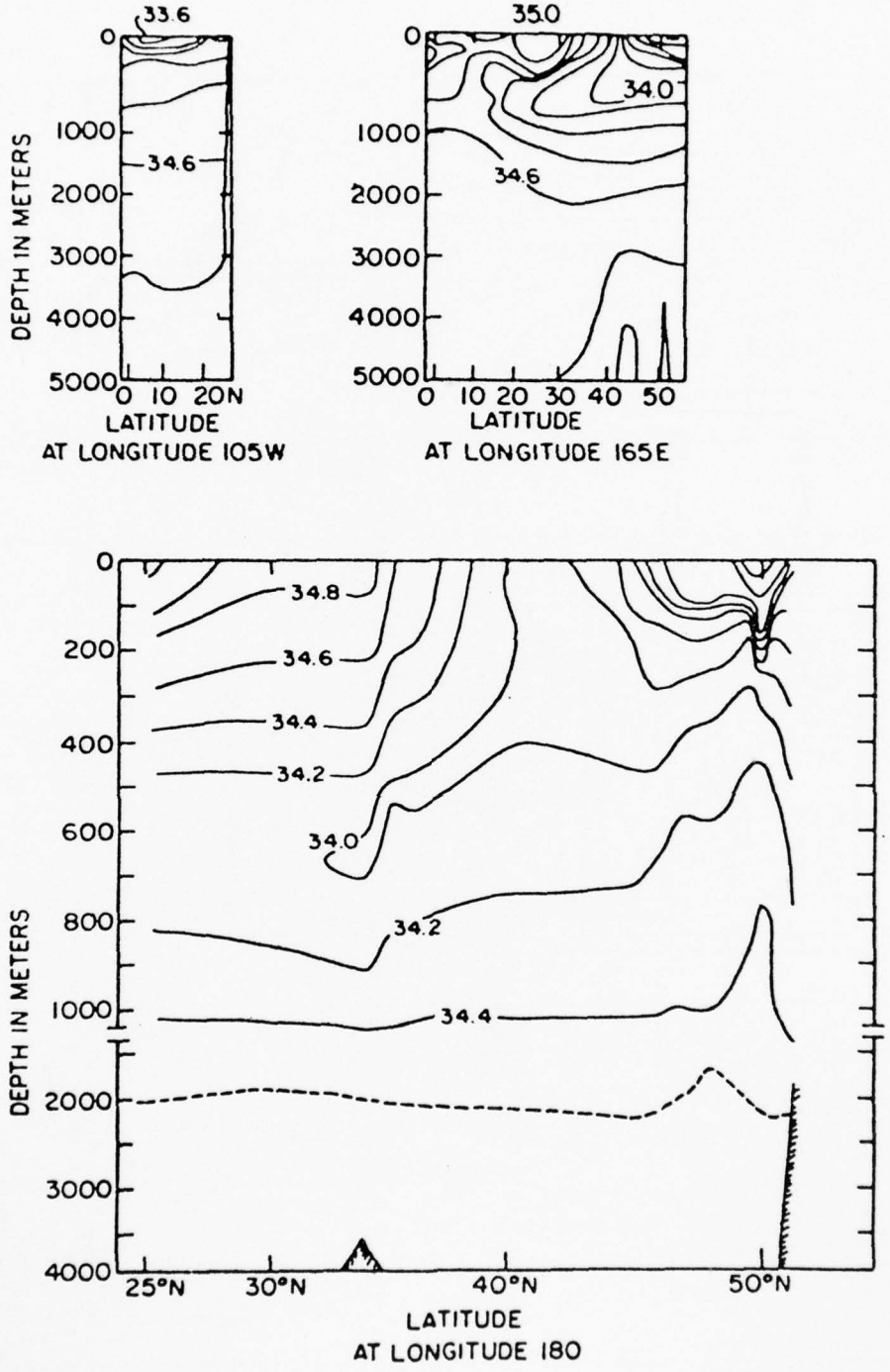

Observed North-South Salinity Profile in the North Pacific Ocean

Figure 24

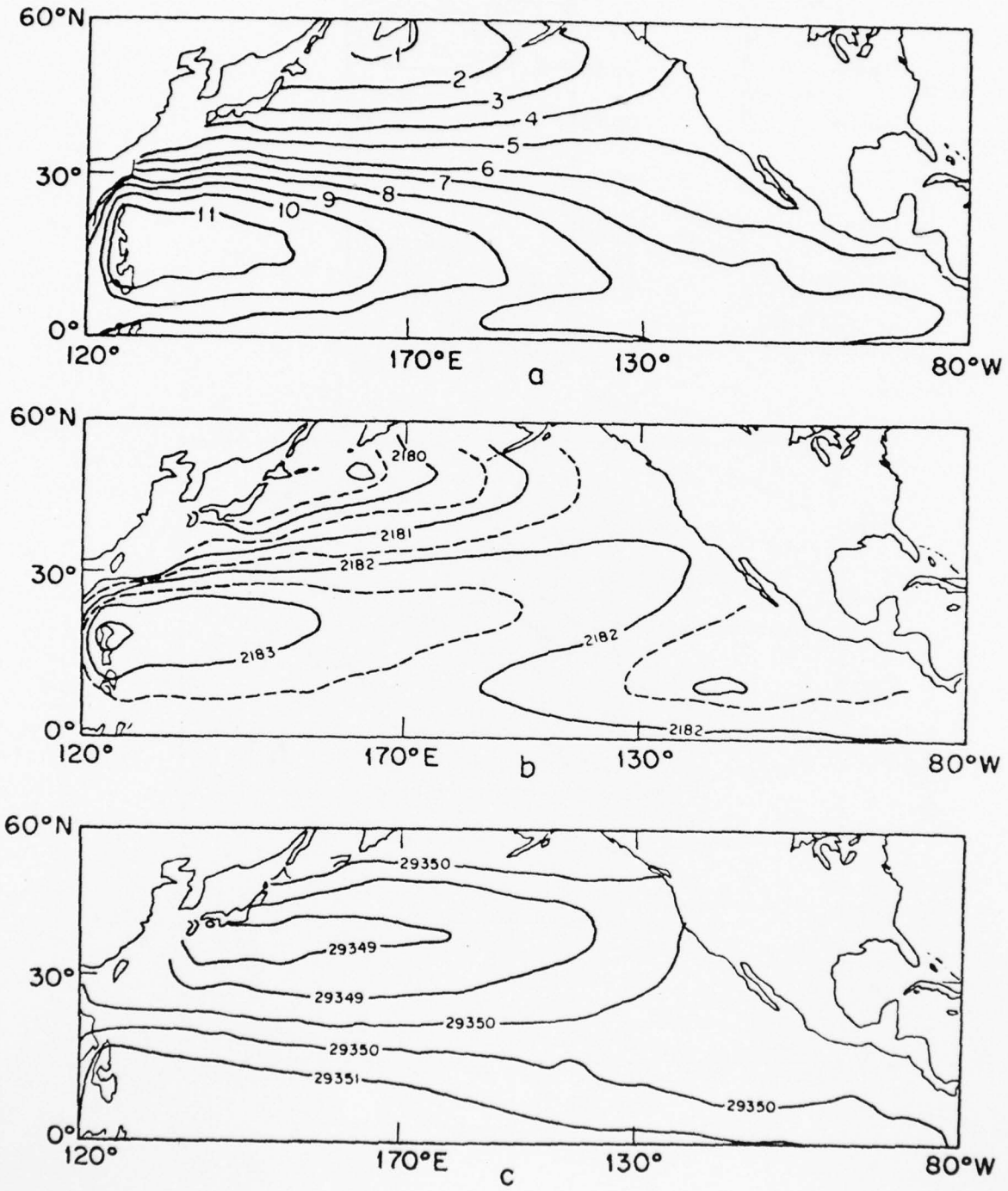
60°N
30°
0°
120°
170°E
130°
80°W
a
2
3
4
5
6
7
8
9
10
11
b
2180
2181
2182
2183
c
29350
29349
29351

Figure 25

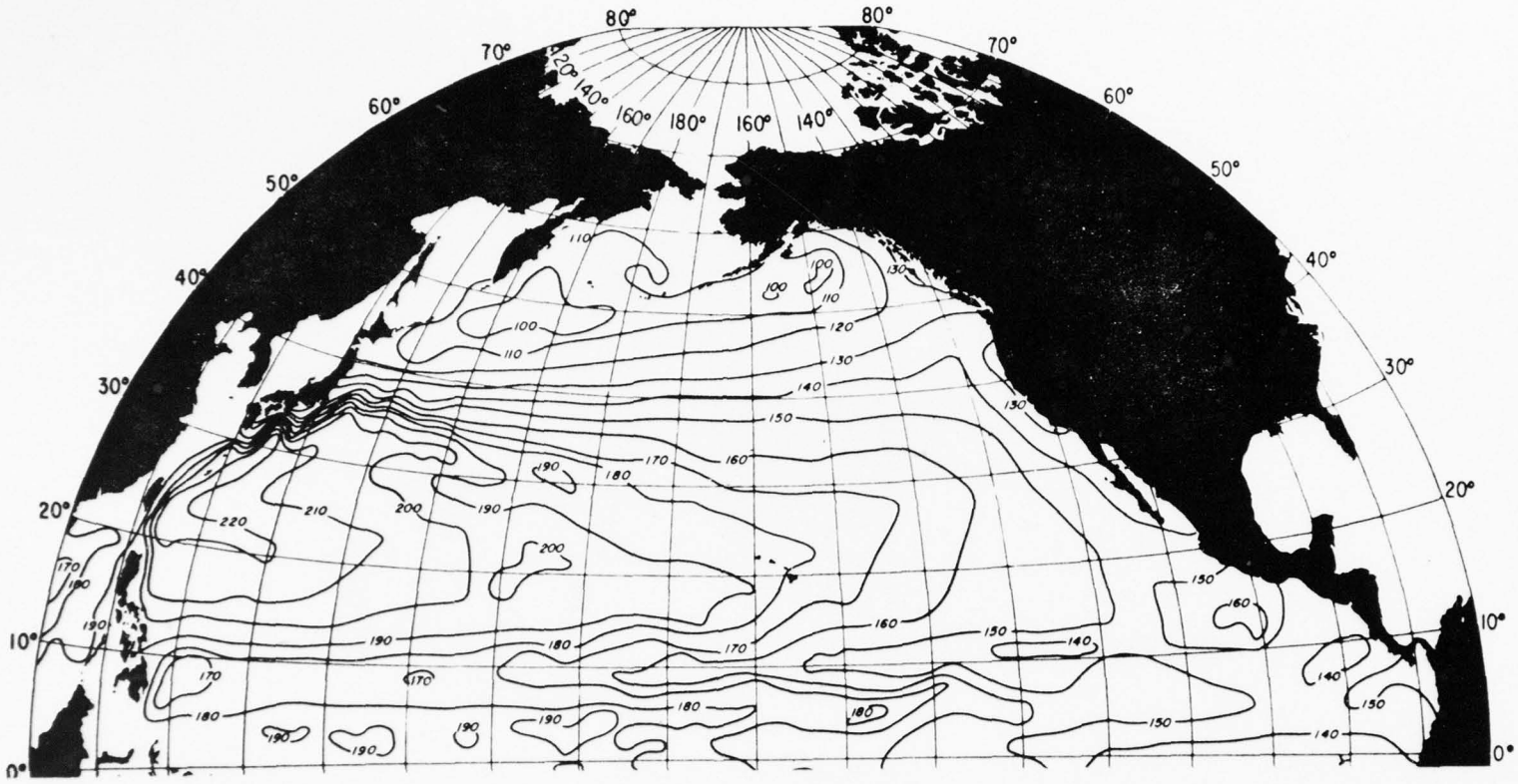
80°
70°
60°
50°
40°
30°
20°
10°
0°
120°
140°
160°
180°
160°
140°
110
100
130
120
150
170
190
210
220
200
180
160
150
140

Figure 26

AD-A072 589 MICHIGAN UNIV ANN ARBOR DEPT OF ATMOSPHERIC AND OCE--ETC F/G 8/10
NUMERICAL SIMULATION STUDIES FOR THE OCEANIC ANOMALIES IN THE N--ETC(U)
FEB 77 J C HUANG N00014-76-C-0141

UNCLASSIFIED NL

2 OF 2
AD A072589

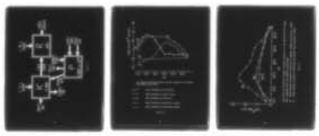

END
DATE FILMED
9-79
DDC

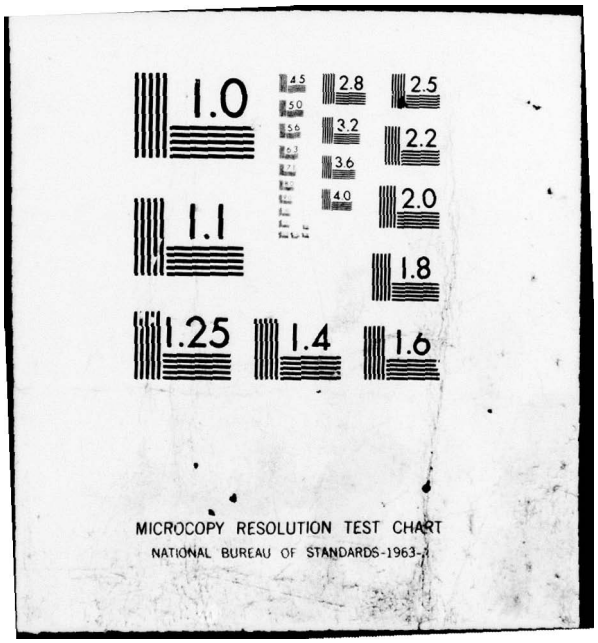
1.0
1.1
1.25
1.4
1.6
1.8
2.0
2.2
2.5
2.8
3.2
3.6
4.0
4.5
5.0
5.6
MICROCOPY RESOLUTION TEST CHART
NATIONAL BUREAU OF STANDARDS-1963-A

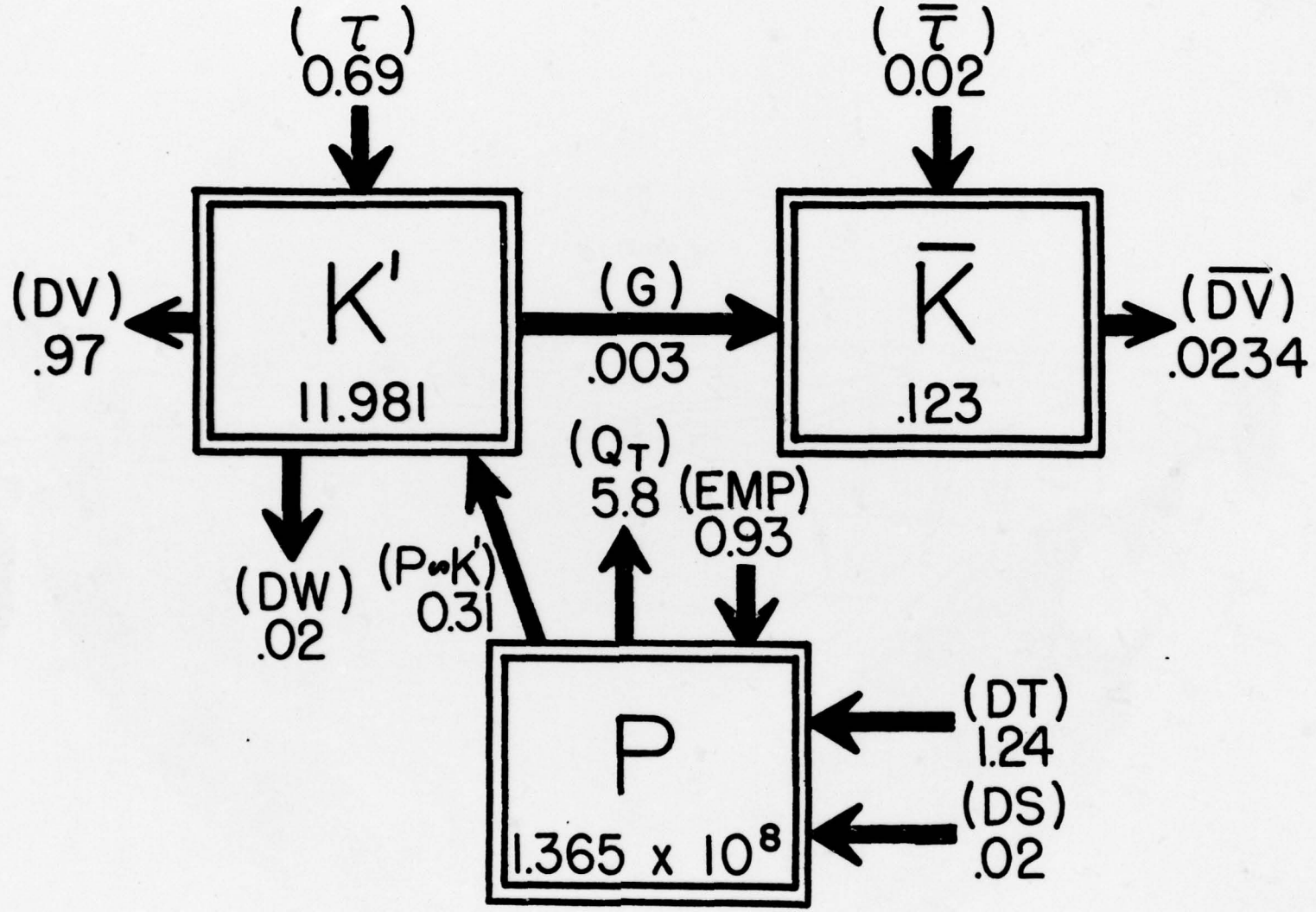
(τ)
0.69
(τ̄)
0.02
(DV)
.97
K'
11.981
(G)
.003
K̄
.123
(DV̄)
.0234
(Q_T)
5.8
(EMP)
0.93
(DW)
.02
(P∞K')
0.31
P
1.365 x 10^8
(DT)
1.24
(DS)
.02

Figure 27

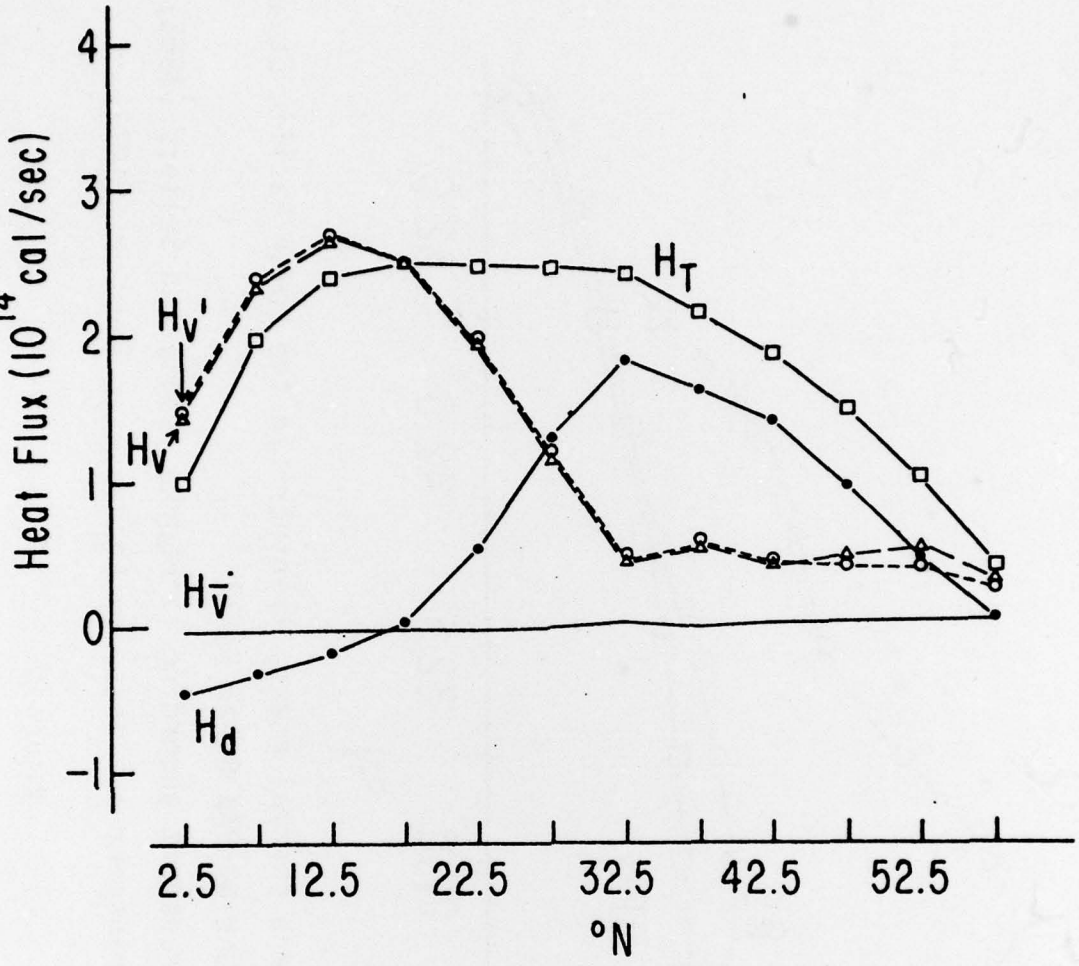

Variation of northward thermal energy transport, calculated from NORPAX Ocean Model

□——□	Total northward heat transport
△– –△	Heat transport by total current
●——●	Heat transport by diffusion
o– – –o	Heat transport by baroclinic current
——	Heat transport by barotropic current

Figure 28

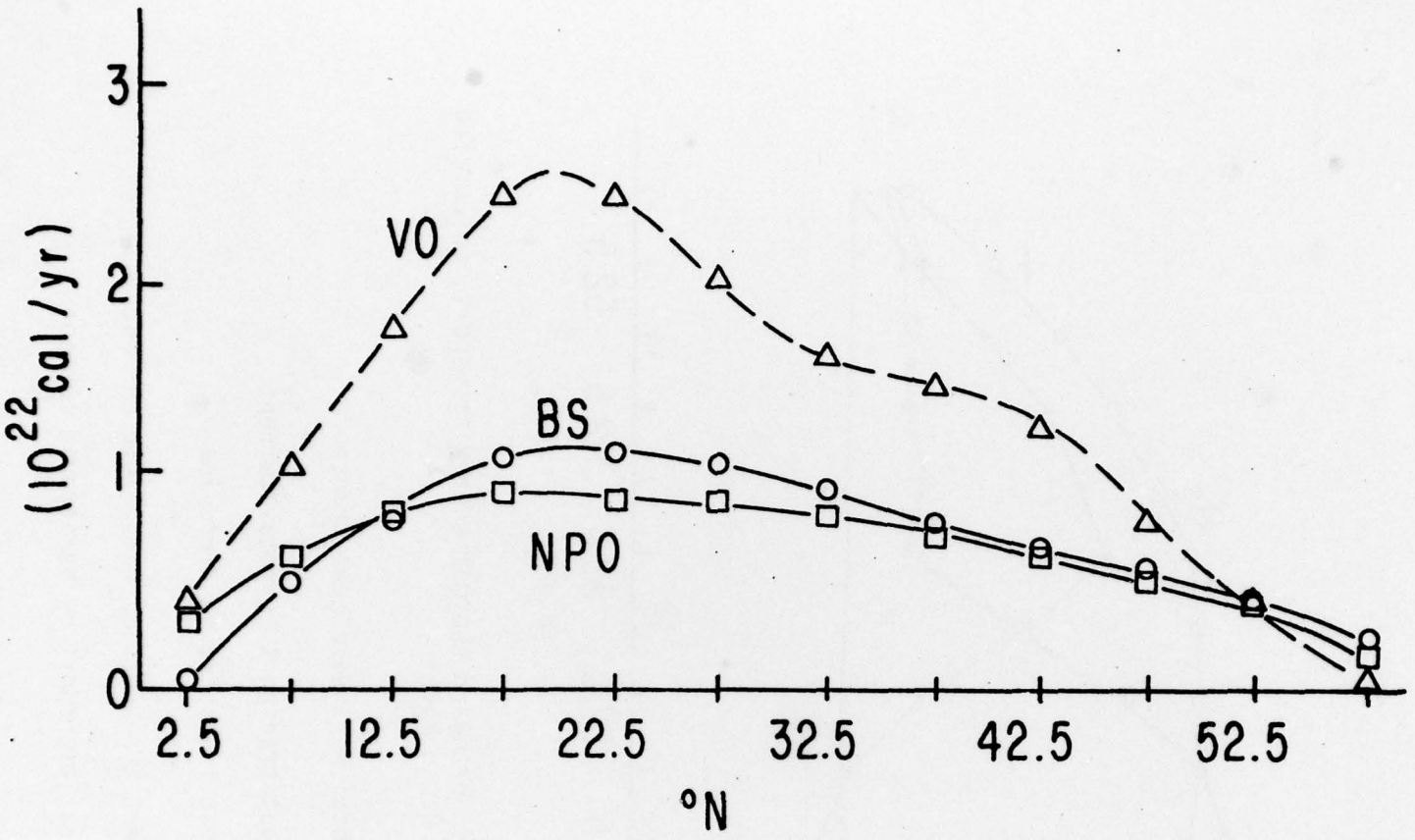

Variation of Northward thermal energy transport in the North Pacific Ocean

NPO computed from the NORPAX Ocean Model

BS Ocean energy transport according to Budyko (1963) and Sellers (1965)

VO Ocean energy transport estimated by Vonder Haar and Oort (1973)

Figure 29